ACCSCIENCE PUBLISHING

International Journal of Bioprinting

RESEARCH ARTICLE

Converging *Pvt1* signaling and 3D bioprinting technology for next-generation biodegradable tracheal replacement constructs

Wei Zuo[1], Shao-Xiao Qiu[2], Jian Cui[1], Wen-Jian Liao[1], Jun-Tao Zou[1], Qing Jie Chen[3]*, and Fei Xu[2]*

[1]Department of Respiratory and Critical Care Medicine, the First Affiliated Hospital of Nanchang University, Nanchang, Jiangxi, China

[2]Department of Respiratory and Critical Care Medicine, Shenzhen Bao'an People's Hospital, Shenzhen, Guangdong, China

[3]Department of Nuclear Medicine, the First Affiliated Hospital of Nanchang University, Nanchang, Jiangxi, China

Abstract

Tracheal reconstruction remains a major clinical challenge due to persistent limitations in graft vascularization, epithelialization, and long-term mechanical compatibility. Conventional synthetic scaffolds and autologous grafts often fail to achieve durable integration, underscoring the need for innovative biofabrication strategies. In the present study, we elucidate the mechanoregulatory role of the long non-coding (lnc) RNA *Pvt1* in controlling endothelial cell proliferation and focal adhesion dynamics during tracheal regeneration. Patient-specific tracheal stents were fabricated using extrusion-based three-dimensional bioprinting with hierarchically optimized architectures that combined polycaprolactone (PCL) copolymers with endothelial progenitor cell (EPC)-recruiting motifs. Computational fluid dynamics-guided nozzle path planning and *in situ* piezoelectric characterization enabled sub-200 μm resolution in replicating native tracheal microtopography while maintaining 94% EPC viability after printing. *Pvt1*-enriched bioinks significantly enhanced vascularization, yielding a 2.3-fold increase in neovascularization compared with controls in rat tracheal defect models, alongside a 38% reduction in fibrotic markers. The constructs exhibited a dual-stage biodegradation profile (30% mass loss at eight weeks), providing mechanical compatibility with tissue ingrowth patterns as confirmed by micro-computed tomography-based strain mapping. Collectively, these findings demonstrate the convergence of lncRNA biology and precision bioprinting, delivering an off-the-shelf solution for complex tracheal reconstruction that addresses current barriers in graft epithelialization and immunomodulatory response. The study advances the translational potential of bioengineered airway substitutes through molecularly informed design principles.

Keywords: Biodegradable materials; Endothelial cells; Personalized treatment; *Pvt1*; Tracheal repair; Three-dimensional printing

***Corresponding authors:**
Qing Jie Chen
(17770879369@163.com)

Fei Xu
(drFeiXuuue@163.com)

Citation: Zuo W, Qiu SX, Cui J, *et al*. Converging *Pvt1* signaling and 3D bioprinting technology for next-generation biodegradable tracheal replacement constructs. *Int J Bioprint*. 2026;12(1):262-282. doi: 10.36922/IJB025160146

Received: April 14, 2025
1st revised: June 26, 2025
2nd revised: August 30, 2025
Accepted: August 9, 2025
Published Online: August 9, 2025

1. Introduction

Tracheal defects represent a life-threatening condition that can arise from surgical trauma, burns, and infections.[1] Clinical manifestations include breathing difficulties, sore throat, coughing, fever, and other severe manifestations.[2] Without timely intervention, tracheal defects pose a serious threat to patient survival and quality of life.[3] Current therapeutic strategies primarily involve tracheal reconstruction surgery or tracheal transplantation.[4] Tracheoplasty employs autologous cartilage or synthetic materials to repair tracheal defects,[5] whereas tracheal transplantation utilizes donor trachea to restore airway continuity.[6] Despite clinical utility, both approaches remain limited. Tracheal reconstruction may result in complications such as cartilage displacement and recurrent laryngeal nerve injury,[7] while transplantation is hindered by immune rejection and a lack of inherent regenerative capacity.[8] These shortcomings underscore the urgent need for more effective and durable treatment strategies.[9]

This study aims to investigate a biotechnology-based therapeutic approach for tracheal defects.[10] Stem cell technology was employed to cultivate tracheal replacement stents with optimized material properties, enhancing biocompatibility and regenerative potential.[11] Additionally, gene editing technology was used to enhance the self-healing ability of tracheal replacement stents and improve their therapeutic efficacy.[12] Such advances hold considerable significance, as the development of an effective biological treatment is expected to transform tracheal defect management by providing safer, more effective, and sustainable options for patients.[13–15]

In recent years, the application of degradable materials in tracheal replacement stents has garnered substantial attention, particularly with the integration of three-dimensional (3D) printing technology into tracheal defect repair.[16,17] Presently, degradable materials mainly encompass polylactic acid, polyhydroxybutyrate, and polycaprolactone (PCL), all degrade *in vivo* without causing adverse effects.[18] Furthermore, 3D printing technology enables precise fabrication of tracheal replacement stents with optimal shape, size, structure, and physical attributes, offering a short production cycle and significant production advantages.[19] Based on these advances, researchers have focused on designing and fabricating biodegradable tracheal replacement stents.[17] Collectively, biodegradable stents represent a promising repair strategy for tracheal defects,[20] and the emergence of 3D printing technology provides a powerful platform for their rational design and scalable production.[21]

Pvt1, a long non-coding RNA located on human chromosome 8q24,[22] spans approximately 1.4 Mb and constitutes a large transcriptional unit comprising 18 exons and 17 introns, with an average exon length of 96 kb.[23] *Pvt1* shows elevated expression across multiple tissues, with particularly high levels in tumor cells.[24] It is also expressed in normal human cells, where its transcription is regulated by diverse signaling pathways, implicating it in a broad range of physiological and pathological processes.[25] Evidence indicates that *Pvt1* exerts critical regulatory functions in cell proliferation, metabolism, and apoptosis.[26] In tumor cells, its overexpression promotes proliferation, invasion, and metastasis.[27] *Pvt1* also plays multifaceted roles in other diseases, such as insulin secretion regulation in diabetes and endothelial function modulation in cardiovascular diseases.[28] Notably, *Pvt1* aggravates airway inflammation and epithelial barrier dysfunction in asthma by regulating miR-149.[29] In addition, *Pvt1* is also involved in interleukin (IL)-1β-induced chondrocyte injury.[30] Given its central roles in diverse disease contexts and its consistently high expression in tumor cells, *Pvt1* is strongly implicated as a key regulator in tracheal defect repair.[26] In the context of tracheal defect repair, *Pvt1* is likely to influence cell proliferation, apoptosis, and differentiation, thereby facilitating the growth and regeneration of tracheal tissue.[26]

In summary, the present study investigates the regulatory role of *Pvt1* in endothelial cell proliferation and adhesion on the luminal surface of a 3D-printed biodegradable tracheal replacement stent. It aims to discern *Pvt1*'s involvement in the tracheal defect repair mechanism mediated by the tracheal replacement stent and explore its scientific and clinical significance. This study offers novel insights and directions for tracheal defect treatment by elucidating the role of endothelial cells. The anticipated findings may drive continued advances in treatment strategies and technological refinement, ultimately improving patient recovery and long-term outcomes.

2. Materials and methods

2.1. Experimental animals

Ten-week-old male F344 rats (n = 112) were purchased from Beijing Vital River Laboratory Animal Technology Co., Ltd. (Beijing, China). All animal experiments were reviewed and approved by the Ethics Committee of the First Affiliated Hospital of Nanchang University. Experimental procedures were conducted strictly in accordance with the Experimental Animal Ethics Committee guidelines, ensuring adherence to principles of animal protection, welfare, and ethics. All protocols complied with national regulations on laboratory animal welfare and ethical use in China.

2.2. Design and three-dimensional printing of polycaprolactone tracheal replacement stent

Polycaprolactone, a widely used biodegradable material, was utilized for the 3D printing of tracheal replacement stents. The stent design was modeled after the native trachea of 10-week-old F344 rats. Printing was performed using the Biomaker system (Beijing Shangpu Bio, China). The printing parameters were as follows: nozzle temperature, 21°C; platform temperature, ambient; printing speed, 5 mm^3/s; initial layer speed, 5 mm^3/s; idle speed, 20 mm^3/s; extrusion speed, 1 mm^3/s; and layer height, 0.2 mm. Continuous blue light illumination was applied throughout the printing process. Immediately after fabrication, the stents were immersed in 2% calcium chloride solution for ionic cross-linking, followed by three washes with phosphate-buffered saline (PBS). To assess the material properties of PCL before and after printing, Fourier-transform infrared spectroscopy (Thermo Fisher, USA) and differential scanning calorimetry (DSC-500T, Shanghai INESA, China) were performed.[31]

The degradation behavior and surface morphology of PCL scaffolds were analyzed at defined time points. Chondrocytes were harvested and resuspended in Dulbecco's Modified Eagle Medium (DMEM; Gibco, USA) supplemented with 10% fetal bovine serum (FBS; Hyclone, USA) at a final concentration of 5.0×10^7 cells/mL. Prior to cell seeding, scaffolds were pre-wetted by immersion in culture medium. Each scaffold was incubated with 2 mL of cell suspension in a 15 mL centrifuge tube under 5% carbon dioxide at 37°C for 30 min, with gentle inversion every 10 min to ensure uniform cell attachment across scaffold surfaces. Scaffolds were then transferred into a six-well culture plate (Becton Dickinson, USA), and 7.5 mL of DMEM containing 10% FBS, 50 μg/mL vitamin C (Sigma-Aldrich, USA), 100 U/mL penicillin, 100 mg/mL streptomycin, and 0.1 mM non-essential amino acids (Invitrogen, USA) was added. After 3 days of static culture, constructs were placed on a shaker at 100 rpm under 5% carbon dioxide at 37°C and cultured for 2–4 weeks. At each time point, scaffolds were vacuum freeze-dried, sputter-coated with gold, and analyzed using scanning electron microscopy (SEM; Quanta 250, FEI, USA).[32]

2.3. Three-point bending test

The mechanical properties of three tracheal replacement stents were evaluated using electronic universal testing machines (INSTRON 3345 and INSTRON 5584; Instron, USA) equipped with Bluehill 3 software. For the three-point bending test, each rectangular or circular cross-sectional specimen was positioned on a bending fixture, the span was adjusted, and the sample was loaded until either the specified bending displacement was reached or the specimen fractured. For rectangular samples, height and width were measured at both ends and at the midpoint of the span. The mean values of the three measurements for width and height were used for analysis. The testing software recorded displacement/load curves, compressive strength,[33] force distribution, and rotation angle.[34]

2.4. Radial compression force measurement

Radial compression tests were performed on three tracheal replacement stents using the HY-940FS computerized tensile and compression testing machine (Shanghai Hengyu, China). The compression rate was set at 2 mm/min, and the radial compression force and percentage of deformation were continuously recorded. Radial compression force–deformation curves were generated for each specimen. All tests were conducted under controlled environmental conditions (temperature 20 ± 1 °C, relative humidity 65 ± 2%).

2.5. Construction of an artificial trachea using *in vitro* cell-alginate hydrogel-polycaprolactone stent structure

The PCL tracheal replacement stent was designed with a longitudinal length of 10 mm and a diameter of 5 mm, corresponding to the average tracheal size of 10-week-old F344 rats. Each stent consisted of five layers. The innermost and outermost layers were constructed from porous PCL mesh to facilitate cell adhesion, proliferation, and neovascularization, whereas the central PCL layer formed a non-porous cylindrical structure to provide mechanical reinforcement. Alginate hydrogel layers were interposed between the PCL layers to spatially separate endothelial and chondrocyte populations. Endothelial cells were isolated from rat pulmonary arteries using a trypsin-collagenase digestion method combined with differential adhesion and cultured in an endothelial cell medium (A0020, Shanghai Yuchun Biotech, China). Chondrocytes were isolated from rat cartilage using type II collagenase digestion and cultured in chondrocyte medium (4651, Shanghai Zhongqiao Xinzhou Biotech, China). Syngeneic cells were used to minimize immune rejection and ensure optimal biocompatibility. Cell morphology was observed daily, and the artificial trachea was imaged using SEM.

2.6. Cell distribution in the three-dimensional-printed artificial trachea

Cell distribution in agarose gels containing alginates was identified using CellTracker™ fluorescent probes (C2925, C2927, Thermo Fisher Scientific Inc., USA). The fluorescent dye was dissolved in DMSO at a final concentration of 10 mM, and serum-free medium was added before heating the solution to 37 °C. Endothelial cells were resuspended in the pre-warmed red dye solution, while chondrocytes

were resuspended in the green dye solution. Both cell suspensions were incubated at 37 °C in a carbon dioxide incubator for 30 min. Following incubation, the cells were centrifuged, the supernatant was removed, and the cell pellets were collected for 3D bioprinting as previously described.[35] Finally, the cells in the artificial trachea were observed under the BX50 optical microscope (Olympus Corporation, Japan) using appropriate optical filters based on the dye color.

2.7. Live/dead assay

Artificial tracheal constructs were cultured in DMEM (PM150210, Wuhan Nuosi Life Science Technology Co., Ltd., China) enriched with 10% FBS, 1% penicillin-streptomycin, 10 μg/mL amphotericin B, and 50 μg/mL gentamicin. Cell viability was assessed on Days 1, 3, 7, and 14 using the Live/Dead Cytotoxicity Kit (L3224; Thermo Fisher Scientific, USA). Staining was performed at 37°C for an hour with Calcium Green-1 AM (1:500) and tetramethylrhodamine ethyl ester (TMRE; 1:100). Images were acquired using confocal laser scanning microscopy (FV3000, Olympus, Japan). For quantitative analysis, the number of live and dead cells in each image was determined using ImageJ software (version 1.53k, NIH, USA). The percentage of viable cells was calculated as the ratio of live cell nuclei (green fluorescence) to the total number of nuclei per image field.

2.8. Construction of rat models with tracheal defects and artificial trachea transplantation

A rat tracheal resection model was established to evaluate the *in vivo* transplantation efficacy of the artificial trachea. Forty-eight rats with normal respiration were randomly assigned into the following four groups ($n = 12$ per group): control group (artificial tracheal implantation without epithelial cell coverage), experimental group (artificial tracheal implantation with epithelial cell coverage), short hairpin (sh)-negative control (NC) group (artificial tracheal implantation with sh-NC-transfected epithelial cells), and sh-*Pvt1* group (artificial tracheal implantation with sh-*Pvt1*-transfected epithelial cells).

Rats were anesthetized and placed in the prone position. A longitudinal midline incision was made along the ventral neck, followed by exposure and incision of the anterior tracheal wall to create the defect. The artificial trachea corresponding to each group was implanted into the defect, and proximal and distal ends of the native trachea were anastomosed using absorbable polydioxanone II sutures (Johnson & Johnson, USA). The surgical site was closed in layers, and rats were allowed to recover spontaneous breathing postoperatively.[32,36,37]

Postoperative tracheal diameter was monitored monthly using X-ray imaging (VXR-9 M, DRGEM, South Korea). Before sacrifice, tracheal morphology was assessed using computed tomography (Brivo 385, GE Healthcare, South Korea) and endoluminal evaluation with a bronchoscope (CV 260 S, Olympus, Japan). Vascular remodeling at the proximal and distal ends of the stent was examined using a Volcano intravascular ultrasound system (s5 Imaging System, Philips Volcano, USA). Measurements were obtained at 1 mm intervals within a 5 mm range, and plaque composition between the stent inner edge and lumen outer boundary was quantified with a virtual histology software (IVUSLab version 3.2, Philips Volcano, USA). Fibrous tissue was classified as green, fibro-fatty tissue as yellow-green, calcified components as white, and necrotic tissue as red. Incomplete stent expansion was defined as a minimum area of <5 mm^2.

2.9. Histopathological examination

To assess tracheal lumen narrowing and epithelialization, the trachea, including adjacent native segments, was dissected from surrounding tissue in rats. Each tracheal ring was sectioned, and the native trachea served as a normal control for gross and histological comparisons.

Samples were fixed in 10% phosphate-buffered formalin, embedded in paraffin, and dried at 65°C for 3 h. After routine deparaffinization and dehydration, tissues were treated sequentially with 10% trichloroacetic acid and 10% potassium dichromate for 40 min each, followed by rinsing in tap water. Sections were then stained with hematoxylin (PT001; Shanghai Bogu Biotechnology Co., Ltd., China) for 8 min and rinsed again. Counterstaining was performed using a mixture of 1% rhodamine B (R21983; Shangbao Biotechnology, China) and 1% eosin (R23166; Shangbao Biotechnology, China) for 40 min. The reaction was terminated with a solution containing 1% acetic acid and 1% ammonium molybdate. Subsequently, a mixture of 1% bright green dye and 1% phosphoric acid was applied to terminate residual staining. Sections were dehydrated through graded ethanol, cleared with xylene, and mounted with neutral resin. Histological changes were observed under an optical microscope (BX50; Olympus Corporation, Japan).[36]

2.10. Immunohistochemical analysis

Formalin-fixed, paraffin-embedded sections were prepared from rat tracheal tissue, including adjacent native segments. Antigen retrieval was performed in 10 mM sodium citrate buffer (pH 6.0) at 95°C for 20 min to expose target proteins. After cooling, sections were blocked with 3% bovine serum albumin (10×; diluted in PBS; Thermo Fisher, USA) for 30 min at room temperature, followed by overnight incubation at 4°C with primary antibodies:

rabbit anti-CD34 (1 μg/mL, Catalog No. PA5-78978, Thermo Fisher, USA) or anti-CD326 (EpCAM; 10 μg/mL, 14-9326-82, Thermo Fisher, USA). After washing with Triton X-100 Surfact-Amps detergent solution (Thermo Fisher, USA), endogenous peroxidase activity was blocked with a peroxidase inhibitor (Thermo Fisher, USA) for 30 min at room temperature. Detection was performed using biotinylated goat anti-rabbit IgG (H+L) horseradish peroxidase secondary antibody (1:500; Biotinylated goat anti-rabbit IgG (H+L), HRP, Catalog No. 65-6140 Invitrogen, USA), followed by streptavidin–biotin complex and colorimetric visualization with 3,3-diaminobenzidine substrate (Thermo Scientific Metal Enhanced DAB Kit; Thermo Fisher, USA). Slides were counterstained with hematoxylin, dehydrated, and mounted for analysis. Imaging was performed under a 40× optical microscope (BX50, Olympus, Japan).[38]

2.11. Masson staining analysis

Paraffin-embedded sections were dewaxed, rehydrated, and rinsed with distilled water. Nuclei were stained with Weigert's hematoxylin for 5–10 min, followed by rinsing. Sections were then stained with Masson's Ponceau acid red solution for 5–10 min, briefly immersed in 2% glacial acetic acid, and differentiated in 1% phosphomolybdic acid solution for 3–5 min. Without rinsing, the sections were stained with aniline blue for 5 min and immersed in 0.2% glacial acetic acid for 1 min. Finally, sections were dehydrated with absolute ethanol, cleared in xylene, and mounted with neutral resin for histological analysis.

2.12. Immunofluorescence analysis

Tracheal sections were cut transversely at a 7–14 μm thickness and mounted on chrome-alum gelatin-coated glass slides for drying. After washing with PBS, the slides were incubated at room temperature with 1% normal serum in PBS containing 0.5% Triton X-100 (pH 7.4) for 30 min. Endothelial cells were labeled with CD202b (TIE2) antibody (1:200; #PA5-116042, Thermo Fisher, USA), and epithelial cells were labeled with 5-hydroxytryptamine rabbit polyclonal antibody (1:10,000; AB_572263, ABClonal, USA) at 37°C for 1 h. Secondary antibodies included mouse anti-β-tubulin and goat anti-rabbit IgG conjugated to Alexa Fluor 594 (red, 1:200; A-11012, Invitrogen, USA) and Alexa Fluor 488 (green, 1:200; A-11008, Invitrogen, USA). Sections were counterstained with 4',6-diamidino-2-phenylindole (blue; No. D1306, Thermo Fisher Scientific, USA) at 37°C for an hour and imaged under a fluorescence microscope (BX53, Olympus, Japan).

2.13. RNA extraction and sequencing

Three rats were randomly selected from the control group and the experimental group, respectively, for the study. Tracheal tissues from the tracheal transplantation site were collected, and total RNA was extracted using Trizol reagent (Invitrogen, USA). Sample concentration and purity were measured using a Nanodrop 2000 spectrophotometer (Nanodrop, USA). Only samples with RNA integrity number ≥7.0 and 28S:18S ratio ≥1.5 were used for sequencing. Library construction and sequencing were performed by CapitalBio Technology (China). A total of 5 μg RNA per sample was processed, and ribosomal RNA was depleted using the Ribo-Zero™ Magnetic Kit (Epicentre Technologies, USA). Library preparation was performed using the NEB Next Ultra RNA Library Prep Kit (NEB, USA). RNA was fragmented into ~300 bp in the NEB Next First Strand Synthesis Reaction Buffer (5×). First-strand complementary DNA (cDNA) was synthesized using reverse transcriptase and random primers, followed by second-strand cDNA synthesis with dUTP-containing buffer (10×). Ends of cDNA fragments were repaired, poly(A) tails were added, and Illumina sequencing adapters were ligated. USER Enzyme (NEB, USA) was used to digest the second strand of cDNA, generating strand-specific libraries. The DNA libraries were amplified, purified, and enriched by polymerase chain reaction (PCR). Library quality was assessed using Agilent 2100 Bioanalyzer (Agilent Technologies, USA), and concentration was determined using the KAPA Library Quantification Kit (KAPA Biosystems, USA). Paired-end sequencing was performed on the Illumina NextSeq CN500 system (Illumina, USA).

2.14. Quality control of sequencing data and alignment to the reference genome

Raw paired-end reads were evaluated using FastQC v0.11.8 (www.bioinformatics.babraham.ac.uk). Illumina sequencing adapters and poly(A) tails were removed with Cutadapt v1.18. Reads containing more than 5% ambiguous bases (N) were excluded using Perl scripts, and those with ≥70% of bases having a quality score >20 were retained using FASTX Toolkit v0.0.13 (http://hannonlab.cshl.edu/fastx_toolkit/). Sequence correction was performed using BBMap (https://sourceforge.net/projects/bbmap/). High-quality reads were then aligned to the rat reference genome using HISAT2 v0.7.12.

2.15. Bioinformatics analysis

Differential gene expression analysis of transcriptome sequencing data was performed using the limma package in R (version 4.2.2). False discovery rate correction was applied to *p*-values, and significantly differentially expressed genes were defined by the thresholds $|\log_2(\text{fold change})| > 1$ and false discovery rate <0.05. The proteins encoded by the top 50 differentially expressed genes were imported into the STRING database (https://cn.string-db.org/) to construct a protein–protein interaction (PPI) network. Key

genes were identified by ranking adjacent nodes within the network. In addition, the distribution of CpG islands within the *Dlk1* promoter region was predicted using the MethPrimer online tool (http://www.urogene.org/cgi-bin/methprimer/methprimer.cgi).

2.16. Lentiviral vector construction and cell grouping

The interference vector pSIH1-H1-copGFP (SI501A-1, System Biosciences, USA) was used to construct lentivirus-based silencing vectors targeting *Pvt1* and *Dlk1*. Lentiviral particles were packaged in HEK-293T cells using a lentivirus packaging kit (Invitrogen, USA). Viral supernatants were collected 48 h after transfection, and the viral titer was determined to be 1×10^8 TU/mL.

The sh-NC sequence was CTGACTGG GATCAATCGAACT, the sh-*Pvt1*-1 sequence was CAAGAAGATGTGGAGAGAGTT, the sh-*Pvt1*-2 sequence was CAAAGGCTGTCCACAAGAAGA, the sh-*Dlk1*-1 sequence was GACGGGAAATTCT GCGAAATA, and the sh-*Dlk1*-2 sequence was CCATCGTCTTTCTCAACAAGT.

Rat endothelial cells were divided into four groups according to the experimental design: sh-NC, sh-*Pvt1*+sh-NC, sh-*Pvt1*+sh-*Dlk1*, and sh-*Pvt1*. Each group was infected with 1 mL of the corresponding lentivirus, and transduction efficiency was assessed 48 h after infection.

2.17. Cell counting Kit-8 assay

Cell proliferation was assessed using a cell counting Kit-8 (CCK-8) assay (Beijing Solarbio Science & Technology Co., Ltd., China). Endothelial cells in the logarithmic growth phase were seeded into 96-well plates at a density of 1×10^4 cells/well and pre-cultured for 24 h. Cells were then transfected according to experimental groupings. At 0, 24, 48, and 72 h post-transfection, 10 μL of CCK-8 reagent was added to each well, followed by incubation at 37 °C for 3 h. Absorbance was measured at 450 nm using a microplate reader (Synergy H1, BioTek, USA), with values reflecting cell proliferation. Growth curves were plotted based on absorbance data. Each experiment was repeated three times.

2.18. Flow cytometry

Endothelial cells were harvested 48 h after transfection for apoptosis analysis. Cells were digested with 0.25% trypsin (Shanghai Yubo Biotechnology Co., Ltd., China), centrifuged, and washed three times with cold PBS. Apoptosis was evaluated using the annexin-V-fluorescein isothiocyanate (FITC) apoptosis detection kit (Biovision, USA). The annexin-V-FITC/propidium iodide staining solution was prepared at a ratio of 1:2:50 (Annexin-V-FITC: propidium iodide: HEPES buffer). A total of 1×10^6 cells were resuspended in 100 μL staining buffer, gently vortexed, and incubated at room temperature for 15 min, followed by the addition of 1 mL HEPES buffer (Wuhan Promega Life Sciences Co., Ltd., China). FITC and propidium iodide fluorescence were excited at 488 nm, and emission was detected using 525 and 620 nm bandpass filters, respectively. Each experiment was repeated three times.

2.19. Quantitative real-time polymerase chain reaction

Total RNA was extracted from rat endothelial cells using TRIzol (ThermoFisher, USA), and the concentration and purity were measured using a NanoDrop2000 spectrophotometer (ThermoFisher, USA). cDNA was synthesized from RNA using the PrimeScript RT reagent kit (Takara, Japan). Gene-specific primers were synthesized by Takara (**Table S1, Supporting Information**). Quantitative real-time PCR was performed using the 7500 Fast Real-Time PCR System (Thermo Fisher Scientific, USA). The thermal cycling conditions were as follows: initial denaturation at 95°C for 10 min, followed by 40 cycles of denaturation at 95°C for 10 s, annealing at 60°C for 20 s, and extension at 72°C for 34 s. *Gapdh* served as an internal reference gene. Relative gene expression levels were calculated using the $2^{-\Delta\Delta Ct}$ method. Each experiment was independently repeated three times.

2.20. Western blot

Total proteins were extracted from cells using radioimmunoprecipitation assay buffer (Beyotime, China). Cells were incubated on ice for 30 min, followed by centrifugation at 8000 × *g* for 10 min at 4°C, and the supernatant was collected. The total protein concentration was determined using a bicinchoninic acid assay kit (ThermoFisher, USA). A total of 50 μg of protein was mixed with 2× sodium dodecyl sulfate sample buffer, heated at 100°C for 5 min, and subjected to sodium dodecyl sulfate–polyacrylamide gel electrophoresis. The separated proteins were transferred onto a polyvinylidene fluoride membrane and blocked with 5% skimmed milk at room temperature for an hour. The membrane was then incubated overnight at 4°C with primary antibodies diluted in buffer: rabbit anti-cyclin-dependent kinase 2 (1:1500; ab32147, Abcam, United Kingdom), anti-proliferating cell nuclear antigen (1:2500; ab92552, Abcam), anti-B-cell lymphoma 2 (1:2000; ab182858, Abcam), anti-Bcl-2-associated protein X (1:1000; ab32503, Abcam), and anti-glyceraldehyde-3-phosphate dehydrogenase (1:10,000; ab181602, Abcam) as an internal reference. After incubation, the membrane was washed thrice using Tris-buffered saline with Tween 20 (10 min each). Subsequently, the membrane was incubated for an hour with horseradish peroxidase-

conjugated goat anti-rabbit IgG H&L secondary antibody (1:2000; ab97051, Abcam) and additional Tris-buffered saline with Tween 20 washes. Equal volumes of solution A and solution B from the enhanced chemiluminescence kit (ABclonal Technology Co., LTD, China) were mixed in the dark and applied to the membrane. Protein bands were visualized using the Bio-Rad image analysis system (Bio-Rad, USA), and band intensities were quantified with Quantity One software (v4.6.2). The relative expression levels of target proteins were normalized to the intensity of the glyceraldehyde-3-phosphate dehydrogenase band. Each experiment was repeated three times, and the average value was calculated.

2.21. Enzyme-linked immunosorbent assay

Cell culture supernatants were collected, and the concentrations of adhesion factors intercellular adhesion molecule 1 (ICAM-1) and vascular cell adhesion protein 1 (VCAM-1) were determined by enzyme-linked immunosorbent assay (ELISA). The ELISA kit for ICAM-1 was purchased from Abcam (United Kingdom), and the kit for VCAM-1 was obtained from Shanghai Jialai Biotech Co., Ltd. (China).

2.22. Methylation-specific polymerase chain reaction

The enrichment of DNA methyltransferases (DNMT1, DNMT3a, and DNMT3b) at the *Dlk1* gene promoter region was examined using a chromatin immunoprecipitation (ChIP) assay kit (Sino Biological Inc., China). When cell confluence reached 70–80%, 1% formaldehyde was added to cross-link proteins and DNA at room temperature for 10 min. DNA was fragmented by sonication (10 s on/10 s off, 15 cycles), followed by centrifugation at 13,000 rpm at 4°C. The supernatant was divided into three tubes and incubated overnight at 4°C with different antibodies: RNA polymerase II rabbit polyclonal antibody (positive control, 1:100; ab238146; Abcam, United Kingdom); rabbit IgG (negative control, 1:100; ab172730; Abcam, United Kingdom); rabbit anti-DNMT1 (1:100; NBP3-15856, Novus Biological, USA); rabbit anti-DNMT3a (1:100; NB100-265, Novus Biological, USA); and rabbit anti-DNMT3b (1:100; NB300-516, Novus Biological, USA). Protein–DNA complexes were precipitated with protein agarose/sepharose beads, centrifuged, and washed to remove nonspecific binding. Cross-links were reversed overnight at 65 °C, and DNA fragments were purified using phenol-chloroform extraction. The promoter region of *Dlk1* was amplified by quantitative PCR using the following primers: forward 5'-AACTCCACAATGGCAAGGCT-3' and reverse 5'-AACGCACACCACGAAGATGT-3'. Methylation-specific primer sequences are provided in **Table S2, Supporting Information**.

2.23. Chromatin immunoprecipitation assay

A ChIP assay was performed using the ChIP kit (Sino Biological Inc., China) to assess the enrichment of DNA methyltransferases (DNMT1, DNMT3a, DNMT3b) in the *Dlk1* gene promoter region. Cells at 70–80% confluence were cross-linked with 1% formaldehyde at room temperature for 10 min. DNA was then fragmented by sonication into appropriate sizes (10-s bursts with 10-s pauses, 15 cycles). The lysates were centrifuged, and the supernatants were divided into three tubes at 4 °C. Each tube was incubated overnight with either a positive control antibody (RNA polymerase II rabbit polyclonal antibody [1:100; ab238146, Abcam, United Kingdom]), a negative control antibody (rabbit IgG [1:100; ab172730, Abcam, United Kingdom]), or antibodies against DNMT1 (1:100; NBP3-15856, Novus Biological, USA), DNMT3a (1:100; NB100-265, Novus Biological, USA), and DNMT3b (1:100; NB300-516, Novus Biological, USA). Immune complexes were precipitated using protein agarose/sepharose beads, centrifuged, and washed to remove nonspecific binding. Cross-links were reversed by overnight incubation at 65°C, followed by phenol-chloroform extraction and DNA purification. Enrichment of the *Dlk1* promoter region was quantified using quantitative PCR with the following primers: forward 5'-AACTCCACAATGGCAAGGCT-3' and reverse 5'-AACGCACACCACGAAGATGT-3'.

2.24. RNA immunoprecipitation assay

The interaction between *Pvt1* and DNMT1, DNMT3a, and DNMT3b proteins was detected using the RNA immunoprecipitation (RIP) Kit (Sai Cheng Biotechnology Co., Ltd., China). Cells were washed with pre-cooled PBS, lysed on ice with radioimmunoprecipitation assay buffer (Beyotime, China), and centrifuged at 12,000 × g for 10 min at 4°C. The supernatant was collected for immunoprecipitation.

Magnetic beads (50 μL) were washed with 100 μL RIP wash buffer, conjugated with 5 μg antibody, and incubated to allow binding. After resuspension in 900 μL RIP wash buffer, 100 μL of cell extract was added and incubated overnight at 4°C. The bead–antibody–protein–RNA complexes were isolated with a magnetic stand, digested with proteinase K, and the RNA was extracted for PCR detection. Antibodies used included rabbit anti-DNMT1 (1:100; NBP3-15856, Novus Biological, USA), rabbit anti-DNMT3a (1:100; NB100-265, Novus Biological, USA), and rabbit anti-DNMT3b (1:100; NB300-516, Novus Biological, USA). Rabbit anti-IgG (1:100; ab172730, Abcam, United Kingdom) was used as the negative control.

2.25. Statistical analysis

All statistical analyses were conducted using the Statistical Package for Social Sciences software version 21.0 (IBM,

USA). Data are presented as mean ± standard deviation (SD). Comparisons between two normally distributed groups were performed using an unpaired Student's *t*-test. Multiple group comparisons were analyzed by one-way analysis of variance, followed by Tukey's post hoc test. A p-value < 0.05 was considered statistically significant.

3. Results

3.1. Three-dimensionally printed biodegradable polycaprolactone tracheal stents

Polycaprolactone is a synthetic biodegradable polymer with potential applications in tissue engineering and is compatible with 3D bioprinting without requiring toxic solvents.[39] In this study, we constructed a 3D-printed tracheal replacement stent using PCL material (Figure 1A). The scaffold was designed with a longitudinal length of 10 mm and a diameter of 5 mm, dimensions based on the average native tracheal size of 10-week-old F344 rats. The construct consisted of five layers, with the innermost and outermost layers formed by porous PCL mesh to enhance cell adhesion, proliferation, and neovascularization. Additionally, a schematic of the three-layer PCL-constructed 3D-printed trachea is shown in **Figure 1B**. To determine the stability of the PCL chemical structure during the 3D printing process of the tracheal replacement stent, we conducted a Fourier-transform infrared spectroscopy analysis. The absorption spectra of raw PCL, 3D-printed scaffolds, and sterilized scaffolds displayed no detectable differences (**Figure 1C**), indicating that neither 3D printing nor sterilization altered the chemical structure of PCL. Thermal performance was further evaluated by differential scanning calorimetry. All three groups demonstrated endothermic peaks at approximately 60°C, consistent with the melting point of PCL (Figure 1D). During the 3D printing process of PCL, the chamber and nozzle were maintained at 90 and 110 °C, respectively. No significant thermal decomposition phenomenon was observed within this temperature range among the three groups. The crystal structure of PCL remained unchanged before and after the 3D printing and sterilization processes. These findings confirm that the adopted 3D printing method reliably preserves the chemical and thermal stability of PCL.

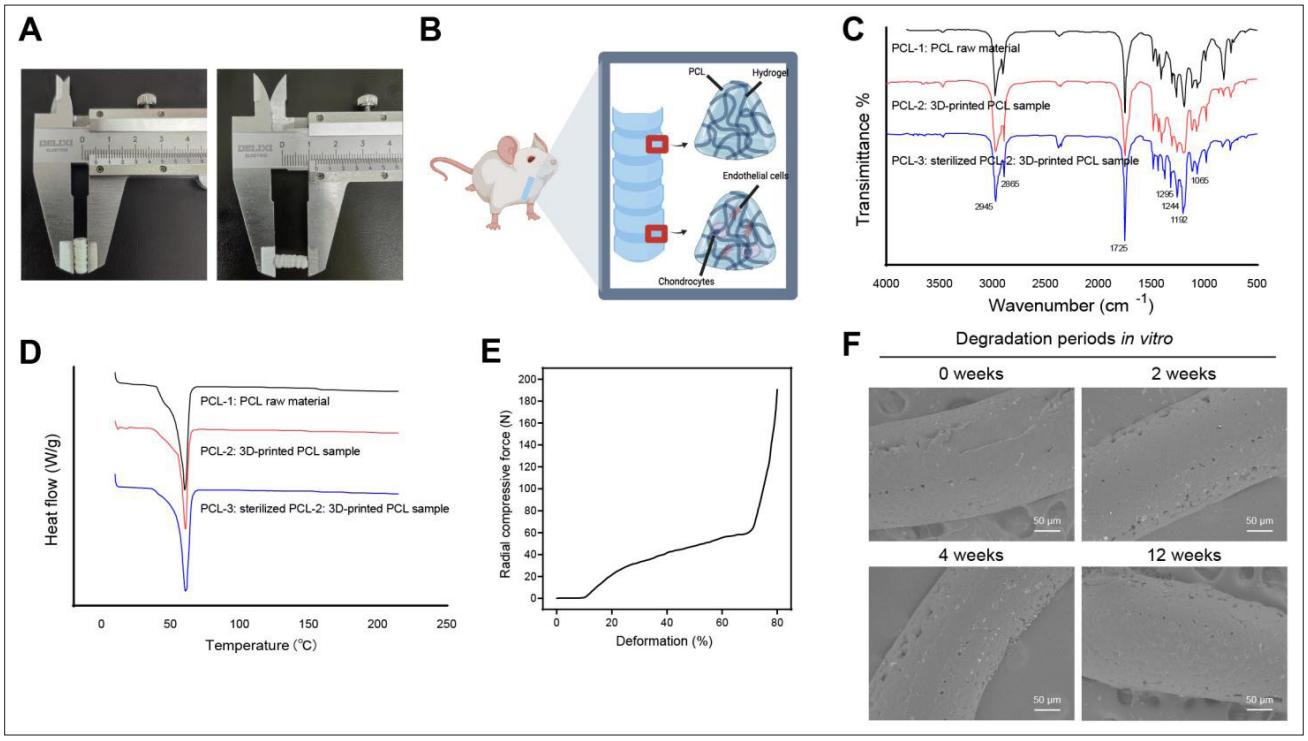

Figure 1. Constructing a degradable PCL tracheal replacement stent using 3D printing. (A) Overview of an artificial tracheal replacement stent fabricated by a 3D bioprinter. (B) Schematic of the three-layer structure of the PCL-constructed 3D-printed trachea. (C) Representative FT-IR spectra of PCL raw materials, 3D-printed PCL samples, and sterilized 3D-printed PCL samples. (D) Differential scanning calorimetry analysis of PCL raw materials, 3D-printed PCL samples, and sterilized 3D-printed PCL samples. (E) Representative radial compression force–deformation curve of the tracheal replacement stent. (F) Scanning electron microscopy observation of PCL tracheal replacement stent after *in vitro* degradation for 2, 4, and 12 weeks. Scale bar: 50 μm; magnification: XX×. All experiments were performed in triplicate. Abbreviations: 3D, three-dimensional; FT-IR, Fourier-transform infrared spectroscopy; PCL, polycaprolactone.

Mechanical properties were evaluated through radial compressive force–deformation testing. Deformation of 10–20% occurred under a compressive force of 20 N, while 70% deformation was observed under 60 N (Figure 1E). The compressive forces corresponding to 10%, 40%, and 70% deformation were 14.52 ± 9.95, 43.20 ± 10.17, and 58.55 ± 11.60 N, respectively. These results demonstrate that the 3D-printed scaffold provides sufficient radial support for *in vivo* transplantation. The three-point bending test confirmed that the scaffold maintained substantial compressive strength (Table S3, Supporting Information).

Scanning electron microscopy (Figure 1F) revealed that the surface morphology of PCL scaffolds remained largely unchanged after *in vitro* degradation for 2, 4, and 12 weeks (Figure 1F). Weight loss analysis showed gradual degradation, with values of 1.1 ± 0.1% at 2 weeks, 2.5 ± 0.2% at 4 weeks, and 5.5 ± 0.2% at 12 weeks. These results indicate that the scaffold degrades slowly while maintaining luminal patency during the early postoperative period.

In summary, a 3D-printed degradable PCL tracheal replacement stent with stable structure, favorable mechanical strength, and controlled degradation was successfully fabricated, establishing a solid foundation for tracheal transplantation.

3.2. Construction of an *in vitro* cell-alginate gel-polycaprolactone tracheal stent

Alginate is a biocompatible and biodegradable material widely applied in tracheal regeneration.[40] In this study, alginate hydrogel was selected as the supporting matrix for cell printing, and both endothelial cells and chondrocytes were incorporated into the scaffold.

Endothelial cells and chondrocytes were successfully isolated from rat tissues (Figure 2A and B). The PCL tracheal replacement stent was designed based on the average tracheal size of 10-week-old F344 rats, with a length of 10 mm, a diameter of 5 mm, and a five-layer structure (Figure 2C). The innermost and outermost PCL layers were fabricated as porous mesh to promote cell adhesion, proliferation, and neovascularization, while the middle layer was a non-porous cylinder providing mechanical strength and separating endothelial cells from chondrocytes. Between each PCL layer, alginate hydrogel was used to embed distinct cell populations (Figure 2D). CellTracker™ staining demonstrated that endothelial cells (red) localized to the inner layer and chondrocytes (green) to the outer layer, with uniform cell distribution throughout the alginate hydrogel (Figure 2E). Cell viability assessed by Live/Dead assay confirmed robust survival: approximately 70% of cells remained viable on Day 1, and viability exceeded 80% from Day 3 onward (Figure 2F). These results indicate the feasibility of constructing an artificial trachea using an extracellular matrix-alginate hydrogel-PCL tracheal replacement stent structure.

3.3. Three-dimensionally printed degradable polycaprolactone tracheal stents with endothelial cell coverage on the inner diameter enhance tracheal defect repair

The re-epithelialization of the long-segment tracheal substitutes depends on the implantation of epithelial cells on the substitutes. In this study, rat endothelial cells were used. To investigate the repair effect of endothelial cells covered on the inner diameter of the degradable PCL tracheal replacement stent fabricated by 3D printing on tracheal defects, a rat tracheal defect model was established, and artificial trachea were implanted at the defect sites. The experimental group received stents with endothelial cells seeded on the inner lumen, whereas the control group received stents without endothelial cell coverage (Figure 3A).

Computed tomography imaging demonstrated that the luminal diameter at the transplantation site was significantly narrowed in the control group, whereas no reduction in luminal diameter was detected in the experimental group (Figure 3B). Bronchoscopic examination confirmed marked stenosis in the control group, with granulomatous tissue partially obstructing the airway, while the experimental group maintained a near-normal luminal diameter and internal morphology (Figure 3C). Histological analysis further supported these findings. Masson's trichrome staining revealed the absence of epithelial regeneration in the control group, accompanied by severe luminal narrowing, whereas the experimental group exhibited consistent *in vivo* regeneration of ciliated epithelial cells covering the inner surface of the stent, closely resembling the structure of a native trachea (Figure 3D). Functional outcomes were further validated by vascular repair analysis. Post-transplantation follow-up (Table S4, Supporting Information) indicated favorable epithelial and vascular regeneration in the experimental group, with no airway obstruction. Ultrasonographic and histological assessment confirmed segmental repair and lumen patency. Immunohistochemical staining reinforced these results: CD34 staining revealed a significant endothelial cell presence in the graft group, consistent with the transplanted vascular endothelial cells, whereas neither normal nor injured trachea exhibited positive staining (Figure 3E). CD326 (EpCAM) staining demonstrated robust regeneration in the graft group, in contrast to minimal epithelial coverage in the injured trachea and normal staining patterns in uninjured tissue. These findings suggest that grafted endothelial cells contributed

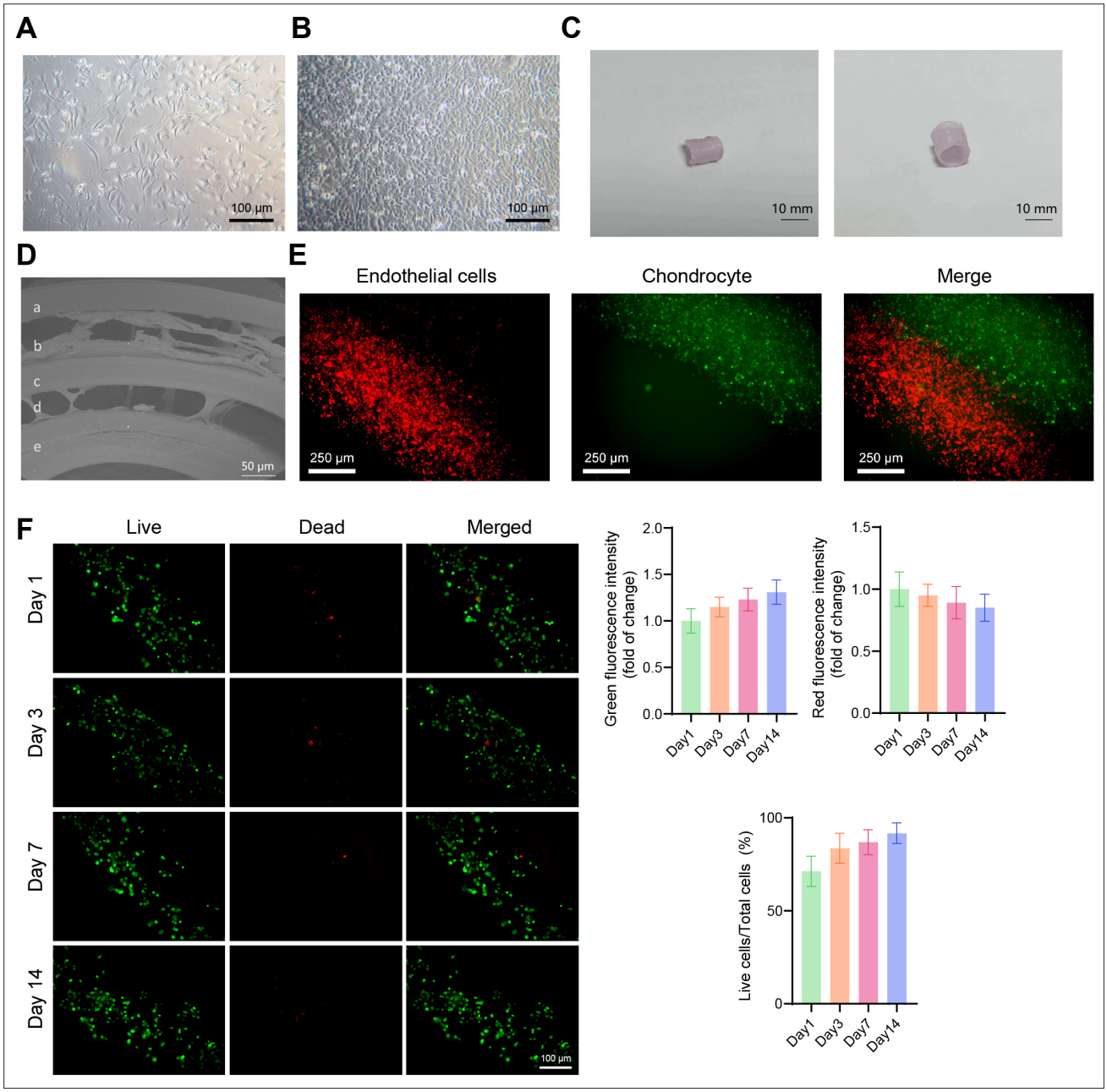

Figure 2. Construction of an *ex vivo* cell-alginate hydrogel-PCL tracheal replacement stent structure. (A) Light microscope morphology of endothelial cells. Scale bar: 100 μm; magnification: 100×. (B) Light microscope morphology of chondrocytes. Scale bar: 100 μm; magnification: 100×. (C) Longitudinal and vertical views of the artificial trachea, with a scaffold length of 10 mm, a five-layer structure, and a diameter of 5 mm. (D) Scanning electron microscopy image showing the enlarged scaffold structure, with layers a, c, and e composed of PCL; layer b composed of alginate gel and chondrocytes; and layer d composed of alginate gel and endothelial cells. Scale bar: 50 μm; magnification: 200x. (E) Observation of the artificial trachea under an optical microscope, with red representing the inner layer of endothelial cells and green representing the outer layer of chondrocytes. Scale bar: 10 μm; magnification: 40x. (F) *In vitro* Live/Dead assay, green and red represent live and dead cells, respectively. Scale bar: 250μm; magnification: 100×. All cellular experiments were repeated three times. Abbreviation: PCL, polycaprolactone.

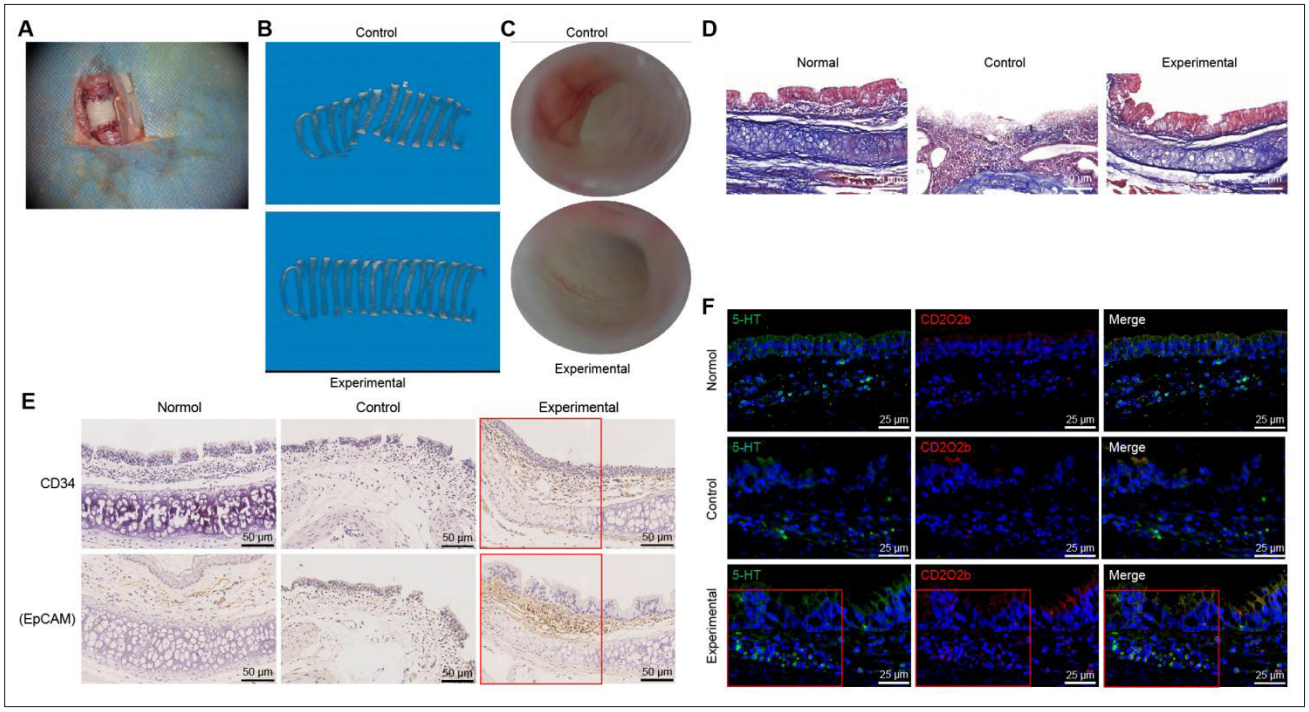

Figure 3. The reparative effect of a 3D-printed degradable PCL tracheal replacement stent with an inner diameter covering endothelial cells on the tracheal injury. (A) Schematic diagram of the artificial tracheal transplantation model. (B) Computed tomography images of rats in the control and experimental groups. (C) Bronchoscope images of rats in the control and experimental groups. Scale bar: 50 μm; magnification: 200×. (D) Masson staining to detect regeneration of epithelial cells in rats in the control and experimental groups, with the native trachea used as a normal control. Scale bar: 50 μm; magnification: 200×. (E) Immunohistochemical staining of CD34 and CD326 (EpCAM) in epithelial and endothelial cells in rats in the control and experimental groups, with the native trachea as a normal control. Scale bar: 50 μm; magnification: 200×. (F) Immunofluorescent staining of 5-hydroxytryptamine (5-HT) in epithelial cells and CD202b in endothelial cells in rats in the control and experimental groups, with the native trachea as a normal control. Scale bar: 25 μm; magnification: 400×. Red boxes highlight the graft scaffold area. 12 rats per group. All cellular experiments were repeated three times.

to epithelial lining repair, potentially through endothelial–epithelial transition (Figure 3E). Immunofluorescence analysis confirmed enhanced epithelial regeneration in the graft group compared to normal and injured trachea, with evidence of endothelial cells differentiating into epithelial cells (Figure 3F).

These results demonstrate that 3D printing of a degradable PCL tracheal replacement stent with an inner diameter covered by endothelial cells can effectively enhance the repair of tracheal defects by the tracheal replacement stent.

3.4. *Pvt1* may affect endothelial cell mesenchymal transition through negative regulation of *Dlk1*

Re-epithelialization of endothelial cells is critical for repairing tracheal injury, and this process is closely associated with cell proliferation and adhesion functions.[41] To investigate the molecular mechanisms underlying endothelial cell transdifferentiation into epithelial cells, transcriptome sequencing was performed on tracheal tissues collected from three rats in both the control and experimental groups. Differential expression analysis identified 267 differentially expressed genes, including 151 downregulated and 116 upregulated genes, with the lncRNA *Pvt1* exhibiting the highest fold change upregulation (Figure 4A and B). Consistent with previous reports, *Pvt1* has been shown to promote endothelial cell proliferation.[42] PPI network analysis of the top 50 differentially expressed genes using the STRING database revealed *Dlk1* as a central node (Figure 4C and D). *Dlk1* expression was significantly downregulated in the experimental group (Figure 4E). Given that *Dlk1* is reported to suppress endothelial cell proliferation,[43] its downregulation suggests a potential role in promoting endothelial–mesenchymal transition during re-epithelialization.

Previous studies have reported that DNA methylation is essential in regulating gene expression in endothelial cells.[44] In the present study, we identified multiple CpG islands within the promoter region of *Dlk1* (Figure 4F), suggesting that its transcriptional activity may be modulated through epigenetic modification. Moreover, evidence indicates that lncRNAs can recruit DNA

methyltransferases (DNMT1, DNMT3a, DNMT3b) to specific promoter regions, thereby modulating DNA methylation and transcriptional activity.[45] Based on these findings, we propose a mechanistic model in which *Pvt1* recruits DNMTs to the *Dlk1* promoter, enhances DNA methylation, and negatively regulates *Dlk1* expression, ultimately facilitating the epithelialization of endothelial cells and contributing to tracheal repair.

3.5. *Pvt1* silencing can downregulate the methylation level of *Dlk1* by reducing the enrichment of DNA methyltransferase in the promoter region of *Dlk1*

We first detected the methylation level of the *Dlk1* promoter CPG island in endothelial cells through Methylation-Specific Polymerase Chain Reaction (MSP) experiments. As shown in Figure 5A, the methylation level of the CpG island in the *Dlk1* promoter region was down-regulated after silencing *Pvt1*. Consistently, ChIP assays revealed that the enrichment of DNMT1, DNMT3a, and DNMT3b at the *Dlk1* promoter was significantly diminished upon *Pvt1* knockdown (Figure 5B). Furthermore, RIP analysis confirmed that *Pvt1* directly interacts with DNA methyltransferases (Figure 5C): after *Pvt1* silencing, the amount of *Pvt1* immunoprecipitated with DNMT1, DNMT3a, and DNMT3b antibodies was markedly reduced. These findings indicate that silencing *Pvt1* may downregulate the methylation level of *Dlk1* by reducing the enrichment of DNA methyltransferases in the *Dlk1* promoter region.

3.6. *Pvt1* silencing can inhibit endothelial cell proliferation and adhesion by upregulating *Dlk1* expression

To investigate whether *Pvt1* regulates endothelial cell proliferation and adhesion via *Dlk1*, endothelial cells were grouped for knockdown experiments. Real-time quantitative PCR analysis confirmed (Figure 6A) that *Pvt1*

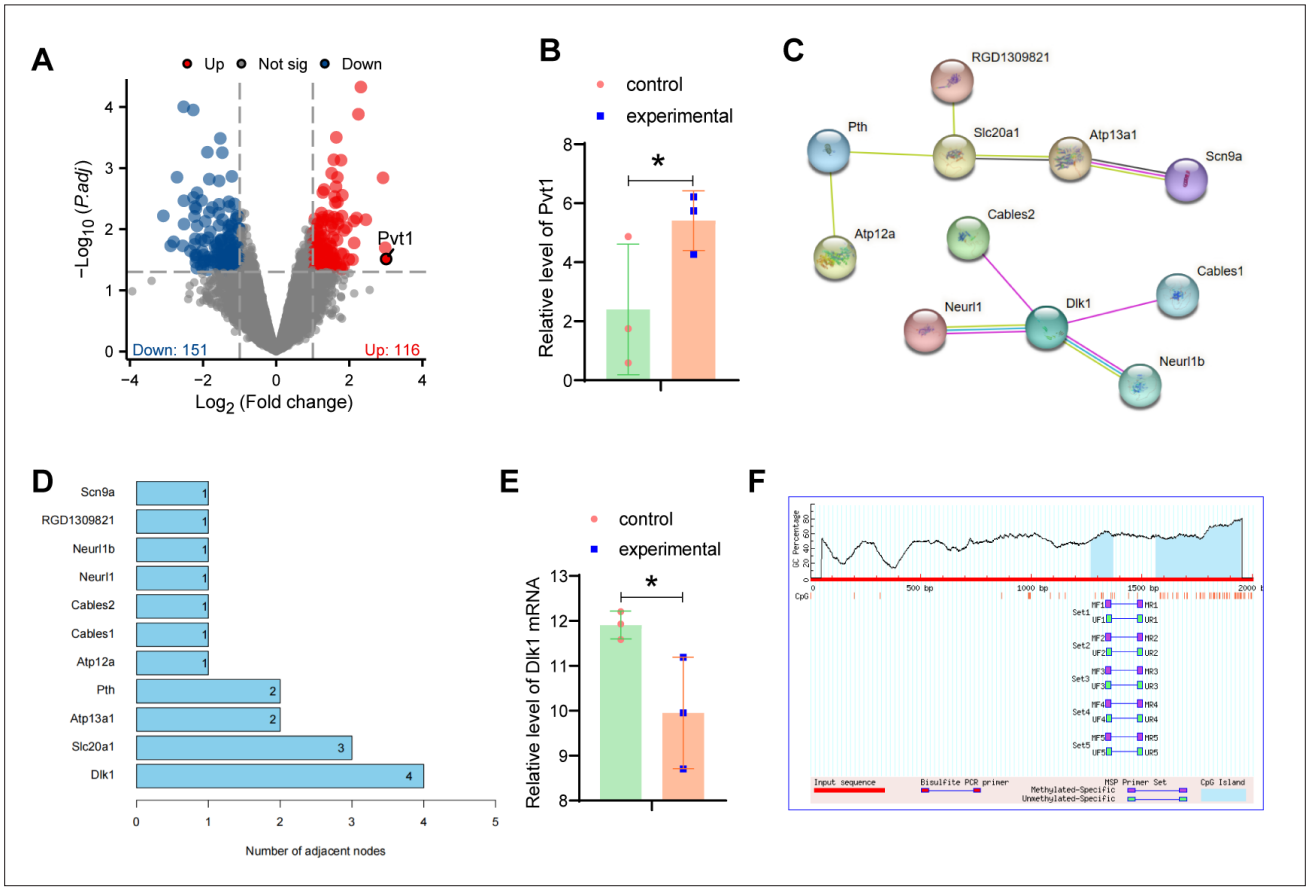

Figure 4. Gene screening through bioinformatics analysis. (A) Volcano plot for differentially expressed genes in the dataset, gray dots represent genes with no differential expression, red dots represent significantly upregulated genes, and blue dots represent significantly down-regulated genes. *Pvt1*, indicated by the plot, represents the gene with the highest upregulation factor. (B) Differential expression of *Pvt1* in tracheal tissues of rats in the control and experimental groups. (C) PPI protein interaction network. (D) Protein interaction adjacent node ranking in the PPI protein interaction network. (E) Differential expression of *Dlk1* in tracheal tissues of rats in the control and experimental groups. (F) Methprimer online website predicts CpG island distribution in the *Dlk1* promoter region. Abbreviation: PPI, protein–protein interaction.

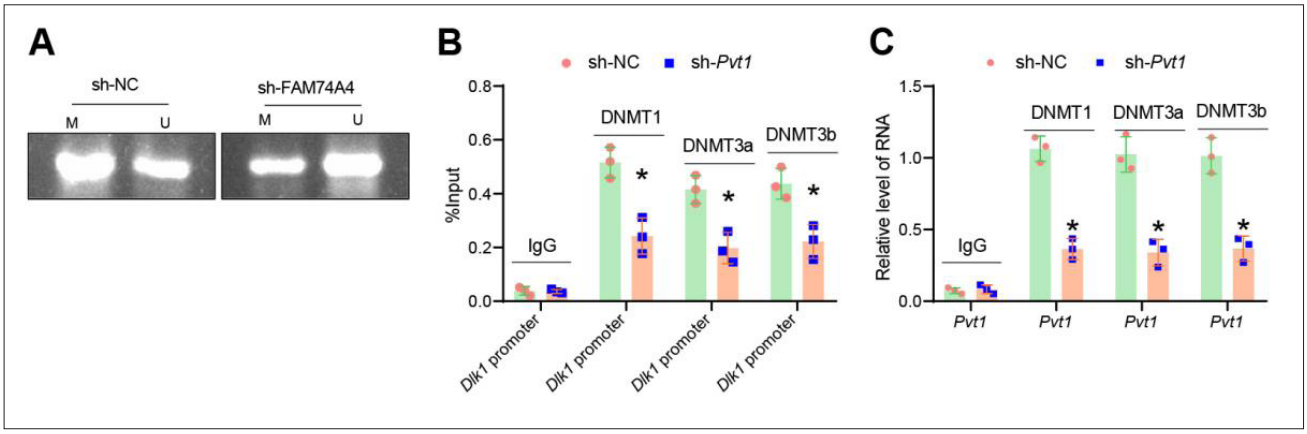

Figure 5. Study on the mechanism of *Pvt1* regulating *Dlk1*. (A) Methylation level detection of CpG island in the *Dlk1* promoter region in endothelial cells using Methylation-Specific Polymerase Chain Reaction (MSP) experiment, with M representing methylated and U representing unmethylated. (B) DNA methyltransferase enrichment detection in the *Dlk1* promoter region using chromatin immunoprecipitation experiment. (C) Binding of *Pvt1* with DNA methyltransferase detection using RNA immunoprecipitation experiment. * indicates a significant difference between the two groups with a *p*-value of less than 0.05. All cell experiments were performed in triplicate. Abbreviations: DNMT, DNA methyltransferase; NC, negative control; sh, short hairpin.

and *Dlk1* were efficiently silenced, with sh-*Pvt1*-2 and sh-*Dlk1*-2 showing the highest knockdown efficiency and therefore selected for further assays. Compared with the sh-NC group, *Pvt1* knockdown significantly reduced *Pvt1* expression and concomitantly increased *Dlk1* expression. In contrast, co-silencing *Dlk1* abrogated this effect, reducing *Dlk1* expression without altering *Pvt1* levels, indicating that *Pvt1* silencing upregulates *Dlk1* expression.

Functional assays further demonstrated the consequences of this regulatory relationship. CCK-8 and flow cytometry analyses showed (Figure 6B and C) that *Pvt1* knockdown significantly inhibited endothelial cell proliferation and promoted apoptosis, while simultaneous silencing of *Dlk1* reversed these effects. Western blotting supported these findings: *Pvt1* silencing decreased cyclin-dependent kinase 2, proliferating cell nuclear antigen, and B-cell lymphoma 2 expression and increased Bcl-2-associated protein X expression, whereas *Dlk1* silencing restored their levels (Figure 6D). Moreover, ELISA revealed that secretion of adhesion molecules ICAM-1 and VCAM-1 was markedly reduced after *Pvt1* knockdown but recovered upon *Dlk1* silencing (Figure 6E). These results indicate that silencing *Pvt1* can inhibit the proliferation and adhesion of endothelial cells by upregulating the expression of *Dlk1*.

3.7. *Pvt1* silencing impairs repair by endothelial-lined three-dimensionally printed tracheal stents

Our *in vitro* findings demonstrated that silencing *Pvt1* reduces endothelial cell proliferation and adhesion. To further examine the *in vivo* consequences of *Pvt1* silencing on tracheal defect repair, endothelial cells with *Pvt1* knockdown were seeded onto the inner diameter of 3D-printed biodegradable PCL tracheal stents and transplanted into tracheal defect sites in rats. Computed tomography imaging revealed (Figure 7A) that the tracheal lumen in the sh-*Pvt1* group was markedly reduced compared with the sh-NC group. Bronchoscopic evaluation (Figure 7B) confirmed severe tracheal narrowing in the sh-*Pvt1* group, accompanied by granulation tissue proliferation and partial airway obstruction. Regarding epithelial regeneration within the artificial trachea, Masson staining (Figure 7C) demonstrated that, compared with the sh-NC group, the regenerated epithelium in the sh-*Pvt1* group was irregular and poorly organized, accompanied by significant narrowing of the tracheal lumen. In addition, analysis of inflammation-related factors revealed that the levels of *Il6* and *Tnfa* were markedly elevated in the sh-*Pvt1* group compared with the sh-NC group (Figure 7D), indicating the occurrence of a pronounced inflammatory response in the newly formed epithelium.

In summary, 3D printing a degradable PCL tracheal replacement stent with an inner diameter covering silencing *Pvt1* in endothelial cells can inhibit the stent's repairing effect on tracheal defects.

4. Discussion

Tracheal defects are rare but potentially life-threatening conditions that can arise from trauma, tracheal malignancies, surgical injuries, or other causes.[1,46] These defects can lead to airway obstruction and, in severe cases, pose a significant risk to the patient's life.[47] Current clinical management strategies mainly include tracheoplasty and tracheal transplantation. Tracheoplasty is generally effective for repairing short-segment tracheal defects, yet

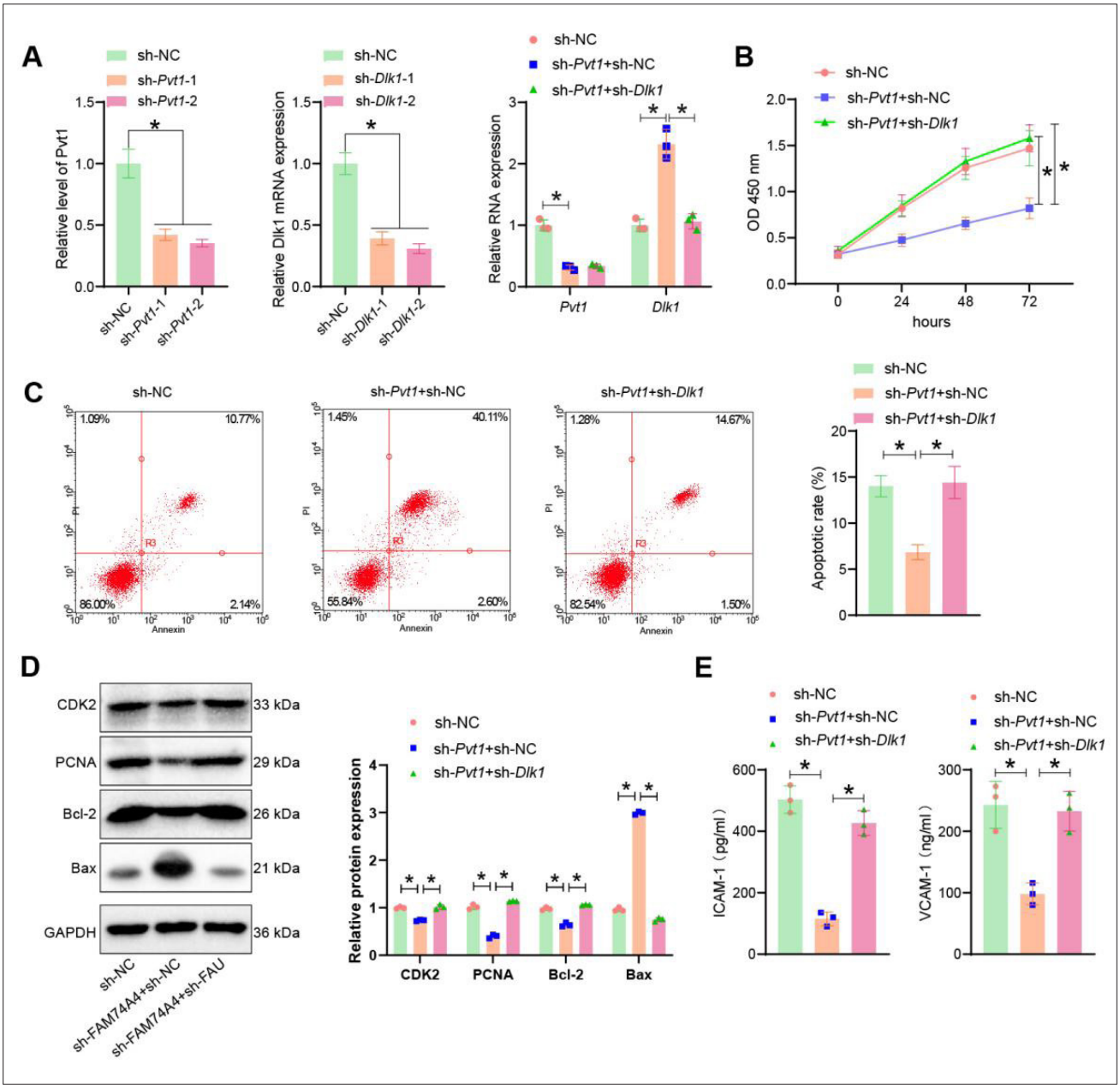

Figure 6. The impact of *Pvt1* on endothelial cell proliferation and adhesion function through regulation of *Dlk1*. (A) Detection of *Pvt1* and *Dlk1* expression levels in cells of each group using real-time quantitative polymerase chain reaction. (B) Assessment of cell proliferation ability in each group using the Cell Counting Kit-8 assay. (C) Measurement of cell apoptosis rate in each group using flow cytometry. (D) Analysis of expression levels of proliferation and apoptosis-related proteins in cells of each group using Western blot. (E) Determination of levels of adhesion factors ICAM-1 and VCAM-1 in the supernatant of cells in each group using enzyme-linked immunosorbent assay. * indicates a significant difference between the two groups with a *p*-value of less than 0.05. All cell experiments were performed in triplicate. Abbreviations: Bax, Bcl-2-associated X protein; Bcl-2, B-cell lymphoma 2; CDK2, cyclin-dependent kinase 2; NC, negative control; PCNA, proliferating cell nuclear antigen; sh, short hairpin.

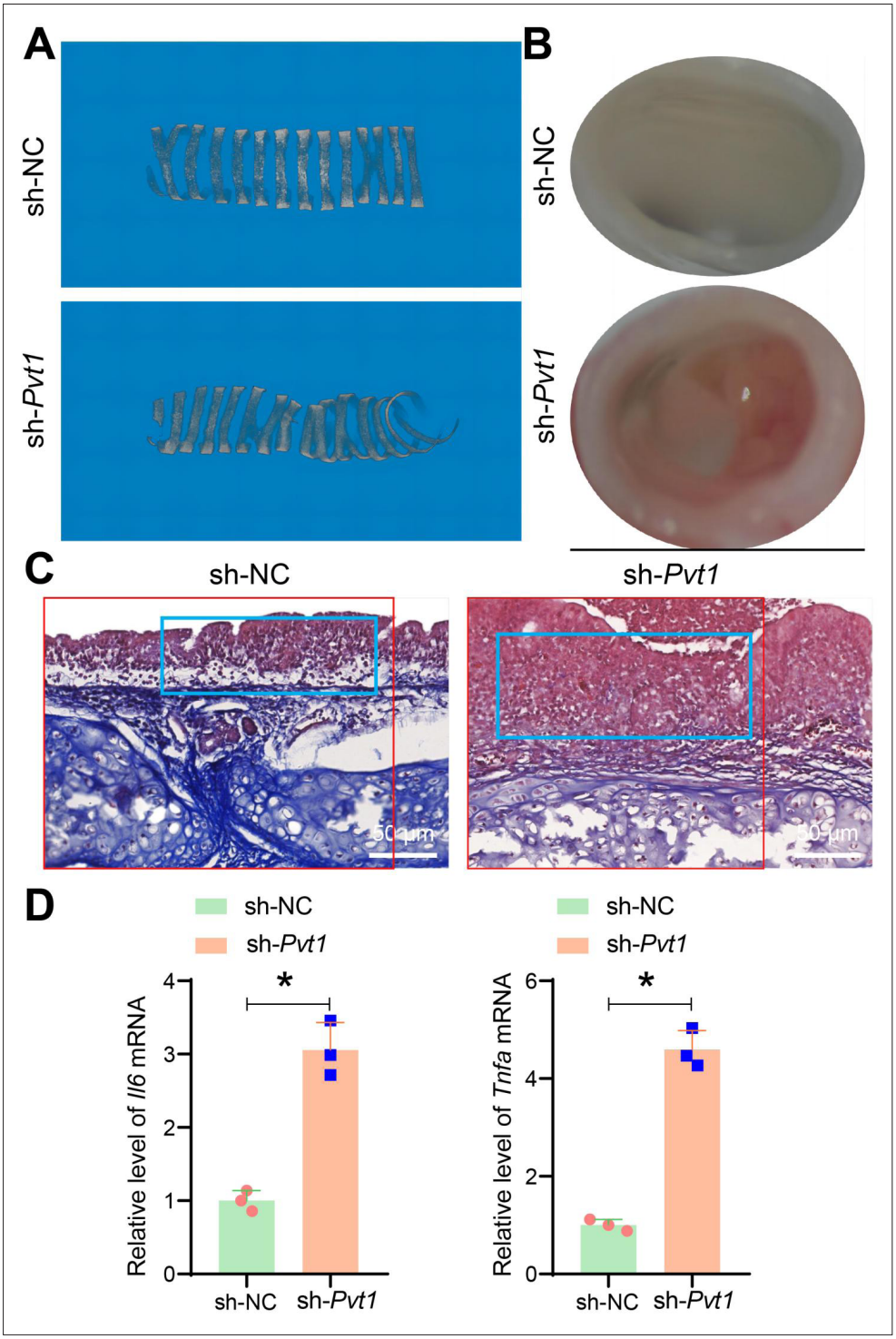

Figure 7. The impact of silencing *Pvt1* on tracheal injury repair in endothelial cells. (A) Computed tomography images of sh-NC and sh-*Pvt1* group rats. (B) Bronchoscopy images of sh-NC and sh-*Pvt1* group rats. (C) Masson staining was used to detect epithelial cell regeneration in the sh-NC and sh-*Pvt1* group rats, with the native trachea serving as a normal control. Scale bar: 50 μm; magnification: 200×. Red boxes highlight the graft scaffold area; (D) Real-time quantitative polymerase chain reaction analysis of *Il6* and levels in cells from sh-NC and sh-*Pvt1* groups, with three independent experiments, * indicates *Tnfas* $p < 0.05$, 12 rats per group. Abbreviations: NC, negative control; sh, short hairpin.

its clinical application is restricted by the complexity of the procedure and the risk of postoperative complications, including tracheomalacia and injury to the recurrent laryngeal nerve.[48] Although progress has been made in tracheal transplantation, major obstacles such as immune rejection and the absence of intrinsic regenerative capacity continue to hinder its widespread clinical adoption.[49–51]

Compared to these traditional treatments, 3D printing provides new solutions for tracheal repair. This method enables precise customization of tracheal replacement stents tailored to a patient's anatomical characteristics, thereby overcoming the limitations of individual variability often encountered with conventional procedures.[52–54] Among the materials available, PCL, a biodegradable polymer, has been widely adopted. PCL-based 3D-printed stents gradually degrade *in vivo* while simultaneously providing mechanical support and facilitating tissue ingrowth, ultimately enhancing repair of tracheal defects. Compared to traditional treatments, 3D-printed tracheal replacement stents have several distinct advantages. First, their porous architecture promotes cell adhesion and proliferation, accelerating tissue reconstruction and regeneration. Second, the structural morphology closely mimics the native trachea, ensuring accurate anatomical fit and physiological functionality. Third, 3D printing enables patient-specific customization, allowing truly personalized treatment. Fourth, as a biodegradable and biocompatible material, PCL provides adequate mechanical strength during the critical repair phase while supporting cell colonization and tissue integration. The long-term goal is that controlled PCL degradation facilitates anastomosis formation and promotes epithelialization through host cell participation.[32,55] Moreover, 3D-printed PCL stents reduce the risk of immune rejection and donor-site complications, while promoting tissue regeneration, further underscoring their clinical promise.[56] Despite these advantages, challenges remain. A significant issue is achieving a balance between the mechanical stability of the scaffold and its biodegradation rate, as premature degradation may compromise airway patency, whereas delayed degradation may impede natural tissue integration. Furthermore, robust clinical evidence is still required to confirm the long-term safety and efficacy of these implants in humans.[32]

In contrast, traditional methods such as tracheoplasty and tracheal transplantation have the following advantages. Tracheoplasty has been shown to achieve satisfactory long-term functional recovery and is supported by a substantial body of clinical data, while tracheal transplantation benefits from a more extended clinical history with relatively well-defined procedures and outcomes. However, these approaches are also limited by notable drawbacks. Tracheoplasty carries inherent risks, including donor site complications and immune rejection, and its technical complexity further restricts its applicability.[57,58] Similarly, tracheal transplantation faces significant challenges related to immune rejection, donor availability, and long-term graft sustainability, which hinder its broader clinical adoption.

This study investigated the role of *Pvt1* in endothelial cell proliferation and adhesion and revealed its potential in repairing tracheal defects using 3D-printed biodegradable PCL tracheal replacement stents. The results demonstrated that 3D-printed biodegradable PCL tracheal stents played a significant role in the repair of tracheal defects, especially when the inner lumen was covered with endothelial cells. It is well established that biological tissues comprise more than one cell type. When tracheal substitute scaffolds are seeded with two or more cell types, they become more similar to native biological tissues, functioning more effectively *in vivo*. In the context of long-segment tracheal defect repair and reconstruction, three critical challenges remain to be addressed: re-epithelialization, revascularization, and neo-cartilage formation.[59] Therefore, endothelial cells and chondrocytes were applied to the tracheal substitute scaffold. Notably, the slow degradation rate of PCL was sufficient to maintain airway patency during the critical early stages of implantation, ensuring structural stability and long-term repair efficacy. Previous studies have shown that the aliphatic ester bonds in PCL are susceptible to hydrolysis, enabling resorption within approximately 24–36 months, coinciding with new tissue growth phases during childhood development.[60] These properties support the suitability of PCL as an ideal material for tracheal replacement. Mechanistically, we further found that *Pvt1* regulates endothelial–mesenchymal transition through modulation of *Dlk1* expression,[43] thereby facilitating tracheal epithelialization and repair. In contrast, silencing *Pvt1* in endothelial cells markedly impaired repair efficacy, underscoring its promotive role in tracheal regeneration.

Moreover, bioinformatics analysis revealed that *Pvt1* negatively regulates endothelial cell mesenchymal transition by modulating *Dlk1*, thereby impacting the effectiveness of tracheal repair. Consistent with earlier studies, *Pvt1* is highly expressed in various tumors and plays a significant role in cell proliferation, invasion, and metastasis.[61] However, despite its significant role in tracheal repair, therapeutic strategies targeting *Pvt1* may pose certain risks by potentially stimulating tumor cell proliferation. Therefore, future research should further explore the dual role of *Pvt1* in different diseases and treatment contexts to develop more refined therapeutic strategies. Given that *Pvt1* is also expressed in normal tissues, molecular markers such as miR-150-5p, octamer-binding transcription factor 4, and c-myc may be valuable indicators for monitoring *Pvt1* activity in cancer-related

contexts.[62,63] Future studies should also explore targeted delivery strategies as a research direction.

Despite the significant advantages of 3D-printed tracheal replacement stents in repairing tracheal defects, several challenges remain. One of the most critical issues is balancing the biodegradation rate and long-term mechanical stability. Excessively rapid degradation may compromise structural integrity, whereas overly slow degradation may hinder tissue remodeling and integration. In our study, degradation assessment at 2, 4, and 12 weeks revealed that PCL tracheal stents underwent relatively rapid degradation during the initial 2 weeks, followed by a more gradual decline. Importantly, even at 12 weeks, the stents retained sufficient mechanical strength and luminal stability to maintain airway patency. To further validate the long-term *in vivo* stability of the material, future investigations should extend the evaluation period to 6 months or even 1 year, if conditions allow. Supplementary indicators such as weight change should also be incorporated to provide a more comprehensive assessment of the degradation profile and mechanical durability. Another key challenge lies in enhancing vascularization of the stent, which is essential for promoting neovascular growth and ensuring long-term survival of the repair site. Ongoing work has begun to explore accelerated aging experiments and long-term follow-up studies to generate more complete data on biodegradation and biocompatibility. Collectively, these findings strengthen the evidence supporting the potential of 3D-printed degradable PCL tracheal replacement stents for tracheal repair and offer new insights and strategies for addressing tracheal defects.

To address these challenges, future research should prioritize several directions. First, the degradation rate and mechanical strength of PCL tracheal replacement stents should be optimized to achieve long-term stability. Second, other biodegradable or composite materials should be explored to enhance the performance of tracheal stents. Third, gene editing and surface modification technologies should be applied to improve immune compatibility and reduce rejection. Fourth, novel therapeutic strategies targeting key molecules such as *Pvt1* and *Dlk1* should be developed to optimize tracheal repair while minimizing potential tumor risks.[26] Additionally, future studies should focus on extending the follow-up time in animal models and conducting more extensive preclinical research to validate the effectiveness of 3D-printed tracheal replacement stents in different clinical scenarios.

This study provides new insights into the role of *Pvt1* in endothelial cell proliferation and adhesion, revealing its potential in tracheal defect repair. By offering new perspectives on tracheal replacement stent design and identifying new therapeutic targets, this study contributes to advancing tracheal repair technologies. Although significant challenges remain, continued technological innovation and a deeper understanding of molecular mechanisms offer strong potential for 3D-printed degradable PCL tracheal replacement stents to emerge as an essential therapeutic option for tracheal defects. Future research should further validate these findings and promote the clinical translation of tracheal repair technologies.[64,59]

5. Conclusion

The present study provides an in-depth evaluation of the potential of 3D-printed degradable PCL tracheal replacement stents for tracheal defect repair and elucidates the role of *Pvt1* in regulating endothelial cell proliferation and adhesion. Through advanced 3D printing technology, personalized tracheal replacement stents were fabricated to closely replicate the anatomical features of the native trachea (**Figure 8**). The use of biodegradable PCL ensured both biocompatibility and predictable degradation. The findings demonstrated that *Pvt1*, a long non-coding RNA, may facilitate tracheal repair by regulating *Dlk1* expression and modulating the endothelial–mesenchymal transition. The interaction between *Pvt1* and *Dlk1* highlights a promising direction for future molecularly targeted interventions. Despite these advantages, challenges remain in balancing long-term mechanical stability with degradation rate, requiring further material optimization and validation. Future research should focus on enhancing stent properties, investigating the therapeutic potential of *Pvt1* and related pathways, and improving the long-term safety and efficacy of tracheal repair. Collectively, these results provide new mechanistic insights and strong technical support for advancing clinical applications in tracheal defect treatment.

Acknowledgments

The authors would like to thank all the colleagues in the Comprehensive Laboratory of the First Affiliated Hospital of Nanchang University for their significant contributions to this research.

Funding

This study was supported by the National Natural Science Foundation of China (82260015), Jiangxi Key Research and Development Plan (No.20243BBI91018), the Jiangxi Provincial Health Commission Science and Technology Project (No.202410200), the Jiangxi Province Traditional Chinese Medicine Science and Technology Project (No.2023A0302), the Shenzhen Baoan People's Hospital academic leader research start-up fund (No.202400120201),

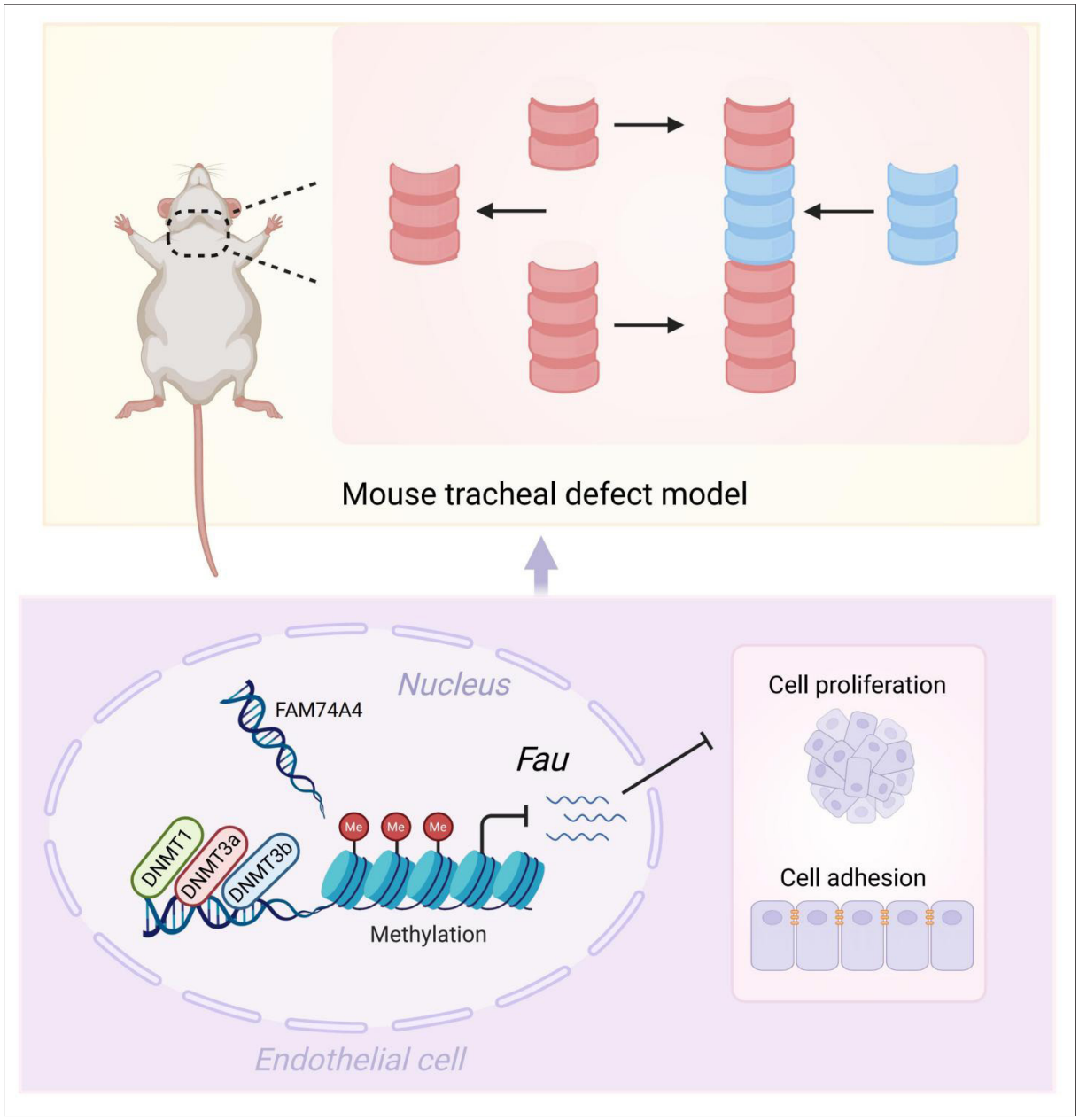

Figure 8. Schematic diagram of the molecular mechanism of three-dimensionally printed biodegradable tracheal replacement stents for repairing tracheal defects. Abbreviation: DNMT, DNA methyltransferase.

and the Shenzhen Baoan District Medical Health Research Project (No.BAGZL2024036).

Conflict of interest

The author(s) declared no potential conflicts of interest concerning the research, authorship, and/or publication of this article.

Author contributions

Conceptualization: W.Z., S.-X.Q., and J.C.
Formal analysis: Q.J.C.
Investigation: J.-L.W. and J.-T.Z.
Methodology: W.Z., S.-X.Q., and J.C.
Supervision: F.X.
Writing–original draft: All authors
Writing–review & editing: All authors

Ethics approval and consent to participate

The experimental and animal study protocols have been approved by the Ethics Committee of the First Affiliated Hospital of Nanchang University.

Consent for publication

Not applicable.

Availability of data

The data supporting this study's findings are available on request from the corresponding author.

References

1. Aydin S, Oz G, Dumanli A, Dongel I, Camas HE. Management of life-threatening tracheal emergencies. *Ann Ital Chir*. 2022;93:626-632.
2. Wang H. Chronic adenoiditis. *J Int Med Res*. 2020;48(11):300060520971458. doi: 10.1177/0300060520971458
3. Filip C, Socolov DG, Albu E, Filip C, Serban R, Popa RF. Serological parameters and vascular investigation for a better assessment in DVT during pregnancy—a systematic review. *Medicina (Kaunas)*. 2021;57(2):160. doi: 10.3390/medicina57020160
4. Sawamoto K, Alvarez Gonzalez J, Piechnik M, *et al*. Mucopolysaccharidosis IVA: diagnosis, treatment, and management. *Int J Mol Sci*. 2020;21(4):1517. doi: 10.3390/ijms21041517
5. Cetrano E, Trezzi M, Secinaro A, *et al*. Bronchial mismatch as a predictor of respiratory failure after congenital tracheal stenosis repair. *Ann Thorac Surg*. 2018;105(4):1264-1271. doi: 10.1016/j.athoracsur.2017.10.046
6. Ren J, Xu Y, Zhiyi G, *et al*. Reconstruction of the trachea and carina: surgical reconstruction, autologous tissue transplantation, allograft transplantation, and bioengineering. *Thorac Cancer*. 2022;13(3):284-295. doi: 10.1111/1759-7714.14315
7. Richardson CM, Hart CK, Johnson KE, Gerber ME. Slide tracheoplasty. *Otolaryngol Clin North Am*. 2022;55(6):1253-1270. doi: 10.1016/j.otc.2022.07.014
8. Zhang S, Xiao G, Peng R, Zhang P, Hong J. Clinical consequences of herpes simplex virus DNA in donor corneas: different prognosis and management of endothelial keratoplasty and deep anterior lamellar keratoplasty. *J Clin Virol*. 2020;129:104508. doi: 10.1016/j.jcv.2020.104508
9. Broersen LHA, Andela CD, Dekkers OM, Pereira AM, Biermasz NR. Improvement but no normalization of quality of life and cognitive functioning after treatment for Cushing's syndrome. *J Clin Endocrinol Metab*. 2019;104(10):4501-4512. doi: 10.1210/jc.2019-01054
10. Wei G, Wang Y, Yang G, Wang Y, Ju R. Recent progress in nanomedicine for enhanced cancer chemotherapy. *Theranostics*. 2021;11(13):6370-6392. doi: 10.7150/thno.57828
11. Shai SE, Lai YL, Hung YW, *et al*. De novo cartilage growth after implantation of a 3-D-printed tracheal graft in a porcine model. *Am J Transl Res*. 2020;12(7):3728-3740.
12. Raguram A, Banskota S, Liu DR. Therapeutic in vivo delivery of gene editing agents. *Cell*. 2022;185(15):2806-2827. doi: 10.1016/j.cell.2022.03.045
13. Perez RE, Santiago JC, Lopez MC, *et al*. Behavior of calcium, phosphorus, and parathormone before transplantation and in months 1, 3, 6, 9, and 12 after transplantation. *Transplant Proc*. 2020;52(4):1152-1156. doi: 10.1016/j.transproceed.2020.01.065
14. Bertolin J, Sanchez V, Ribera A, *et al*. Treatment of skeletal and non-skeletal alterations of mucopolysaccharidosis type IVA by AAV-mediated gene therapy. *Nat Commun*. 2021;12(1):4944. doi: 10.1038/s41467-021-25697-y
15. Chang NW, Dai HJ, Shih YY, *et al*. Biomarker identification of hepatocellular carcinoma using a methodical literature mining strategy. *Database (Oxford)*. 2017;2017:bax082. doi: 10.1093/database/bax082
16. Wu J, Lee B, Saha P, Kumta PN. A feasibility study of biodegradable magnesium–aluminum–zinc–calcium–manganese (AZXM) alloys for tracheal stent application. *J Biomater Appl*. 2019;33(8):1080-1093. doi: 10.1177/0885328218824775
17. Luffy SA, Wu J, Kumta PN, Gilbert TW. Evaluation of magnesium alloys for use as an intraluminal tracheal for pediatric applications in a rat tracheal bypass model. *J Biomed Mater Res B Appl Biomater*. 2019;107(6):1844-1853. doi: 10.1002/jbm.b.34277
18. Wu DT, Munguia-Lopez JG, Cho YW, *et al*. Polymeric scaffolds for dental, oral, and craniofacial regenerative medicine. *Molecules*. 2021;26(22):7043. doi: 10.3390/molecules26227043
19. Gao C, Lu C, Jian Z, *et al*. 3D bioprinting for fabricating artificial skin tissue. *Colloids Surf B Biointerfaces*. 2021;208:112041. doi: 10.1016/j.colsurfb.2021.112041
20. Stramiello JA, Mohammadzadeh A, Ryan J, Brigger MT. The role of bioresorbable intraluminal airway stents in pediatric tracheobronchial obstruction: a systematic review. *Int J Pediatr Otorhinolaryngol*. 2020;139:110405. doi: 10.1016/j.ijporl.2020.110405
21. Feuerbach T, Kock S, Thommes M. Slicing parameter optimization for 3D printing of biodegradable drug-eluting tracheal stents. *Pharm Dev Technol*. 2020;25(6):650-658. doi: 10.1080/10837450.2020.1727921

22. Yao W, Li S, Liu R, *et al*. Long non-coding RNA PVT1: a promising chemotherapy and radiotherapy sensitizer. *Front Oncol*. 2022;12:959208.
doi: 10.3389/fonc.2022.959208

23. Dvorak P, Leupen S, Soucek P. Functionally significant features in the 5′ untranslated region of the ABCA1 gene and their comparison in vertebrates. *Cells*. 2019; 8(6):623.
doi: 10.3390/cells8060623

24. Shi Y, Yang F, Wei S, Xu G. Identification of key genes affecting results of hyperthermia in osteosarcoma based on integrative ChIP-seq/TargetScan analysis. *Med Sci Monit*. 2017;23:2042-2048.
doi: 10.12659/msm.901191

25. Zhou C, Yi C, Yi Y, *et al*. LncRNA PVT1 promotes gemcitabine resistance of pancreatic cancer via activating Wnt/β-catenin and autophagy pathway through modulating the miR-619-5p/Pygo2 and miR-619-5p/ATG14 axes. *Mol Cancer*. 2020;19(1):118.
doi: 10.1186/s12943-020-01237-y

26. Chen S, Shen X. Long noncoding RNAs: functions and mechanisms in colon cancer. *Mol Cancer*. 2020;19(1):167.
doi: 10.1186/s12943-020-01287-2

27. Zhang M, Zhang L, Fu L, *et al*. Positive feedback regulation of lncRNA PVT1 and HIF2α contributes to clear cell renal cell carcinoma tumorigenesis and metastasis. *Oncogene*. 2021;40(37):5639-5650.
doi: 10.1038/s41388-021-01971-7

28. Shang R, Lal N, Lee CS, *et al*. Cardiac-specific VEGFB overexpression reduces lipoprotein lipase activity and improves insulin action in rat heart. *Am J Physiol Endocrinol Metab*. 2021;321(6):E753-E765.
doi: 10.1152/ajpendo.00219.2021

29. Ma L, Zhang Q, Hao J, Wang J, Wang C. LncRNA PVT1 exacerbates the inflammation and cell-barrier injury during asthma by regulating miR-149. *J Biochem Mol Toxicol*. 2020;34(11):e22563.
doi: 10.1002/jbt.22563

30. Lu X, Yu Y, Yin F, *et al*. Knockdown of PVT1 inhibits IL-1β-induced injury in chondrocytes by regulating miR-27b-3p/TRAF3 axis. *Int Immunopharmacol*. 2020;79:106052.
doi: 10.1016/j.intimp.2019.106052

31. Gao B, Jing H, Gao M, *et al*. Long-segmental tracheal reconstruction in rabbits with pedicled tissue-engineered trachea based on a 3D-printed scaffold. *Acta Biomater*. 2019;97:177-186.
doi: 10.1016/j.actbio.2019.07.043

32. Gao M, Zhang H, Dong W, *et al*. Tissue-engineered trachea from a 3D-printed scaffold enhances whole-segment tracheal repair. Sci Rep. 2017;7(1):5246.
doi: 10.1038/s41598-017-05518-3

33. Park HS, Lee JS, Jung H, *et al*. An omentum-cultured 3D-printed artificial trachea: in vivo bioreactor. *Artif Cells Nanomed Biotechnol*. 2018;46(suppl 3):1131-1140.
doi: 10.1080/21691401.2018.1533844

34. Ahn CB, Son KH, Yu YS, Kim TH, Lee JI, Lee JW. Development of a flexible 3D printed scaffold with a cell-adhesive surface for artificial trachea. *Biomed Mater*. 2019;14(5):055001.
doi: 10.1088/1748-605X/ab2a6c

35. Bae SW, Lee KW, Park JH, *et al*. 3D bioprinted artificial trachea with epithelial cells and chondrogenic-differentiated bone marrow-derived mesenchymal stem cells. *Int J Mol Sci*. 2018;19(6):1624.
doi: 10.3390/ijms19061624

36. Park JH, Yoon JK, Lee JB, *et al*. Experimental tracheal replacement using 3-dimensional bioprinted artificial trachea with autologous epithelial cells and chondrocytes. *Sci Rep*. 2019;9(1):2103.
doi: 10.1038/s41598-019-38565-z

37. Taniguchi D, Matsumoto K, Tsuchiya T, *et al*. Scaffold-free trachea regeneration by tissue engineering with bio-3D printing. *Interact Cardiovasc Thorac Surg*. 2018;26(5):745-752.
doi: 10.1093/icvts/ivx444

38. Jensen EC. Quantitative analysis of histological staining and fluorescence using ImageJ. *Anat Rec (Hoboken)*. 2013;296(3):378-381.
doi: 10.1002/ar.22641

39. Kaye R, Goldstein T, Grande DA, Zeltsman D, Smith LP. A 3-dimensional bioprinted tracheal segment implant pilot study: rabbit tracheal resection with graft implantation. *Int J Pediatr Otorhinolaryngol*. 2019;117: 175-178.
doi: 10.1016/j.ijporl.2018.11.010

40. Lee KY, Mooney DJ. Alginate: properties and biomedical applications. *Prog Polym Sci*. 2012;37(1):106-126.
doi: 10.1016/j.progpolymsci.2011.06.003

41. Liu M, Liu Z, Chen Y, *et al*. Dendritic epidermal T cells secreting exosomes promote the proliferation of epidermal stem cells to enhance wound re-epithelialization. *Stem Cell Res Ther*. 2022;13(1):438.
doi: 10.1186/s13287-022-02783-6

42. Zheng J, Hu L, Cheng J, *et al*. lncRNA PVT1 promotes the angiogenesis of vascular endothelial cell by targeting miR-26b to activate CTGF/ANGPT2. *Int J Mol Med*. 2018;41(3):1742-1752.
doi: 10.3892/ijmm.2018.3595

43. Schober A, Nazari-Jahantigh M, Wei Y, *et al*. MicroRNA-126-5p promotes endothelial proliferation and limits atherosclerosis by suppressing Dlk1. *Nat Med*. 2014;20(4):368-376.
doi: 10.1038/nm.3487

44. Shirodkar AV, St Bernard R, Gavryushova A, *et al*. A mechanistic role for DNA methylation in endothelial cell-enriched gene expression: relationship with DNA replication timing. *Blood*. 2013;121(17): 3531-3540.
doi: 10.1182/blood-2013-01-479170

45. Herman AB, Tsitsipatis D, Gorospe M. Integrated lncRNA function upon genomic and epigenomic regulation. *Mol Cell*. 2022;82(12):2252-2266.
doi: 10.1016/j.molcel.2022.05.027

46. Welter S, Essaleh W. Management of tracheobronchial injuries. *J Thorac Dis*. 2020;12(10):6143-6151.
doi: 10.21037/jtd-2019-as-05

47. Frauenfelder C, Maughan E, Kenth J, *et al*. Tracheal resection for critical airway obstruction in Morquio A syndrome. *Case Rep Pediatr*. 2023;2023:7976780.
doi: 10.1155/2023/7976780

48. Leivaditis V, Skevis K, Mulita F, *et al*. Advancements in the management of postoperative air leak following thoracic surgery: from traditional practices to innovative therapies. *Medicina (Kaunas)*. 2024;60(5):802.
doi: 10.3390/medicina60050802

49. Genden EM, Laitman BM. Human tracheal transplantation. *Transplantation*. 2023;107(8):1698-1705.
doi: 10.1097/TP.0000000000004509

50. Delaere P, Meulemans J, Vranckx J, Vos R, Poorten VV. Tracheal transplantation. *Thorac Surg Clin*. 2025;35(1):131-141.
doi: 10.1016/j.thorsurg.2024.07.002

51. Samat AA, Hamid ZAA, Yahaya BH. Tissue engineering for tracheal replacement: strategies and challenges. *Adv Exp Med Biol*. 2022;137:137-163.
doi: 10.1007/5584_2022_707

52. Tracy T, Wu L, Liu X, Cheng S, Li X. 3D printing: Innovative solutions for patients and pharmaceutical industry. *Int J Pharm*. 2023;631:122480.
doi: 10.1016/j.ijpharm.2022.122480

53. Uchida DT, Bruschi ML. 3D printing as a technological strategy for the personalized treatment of wound healing. *AAPS PharmSciTech*. 2023;24(1):25.
doi: 10.1208/s12249-023-02503-0

54. Serrano DR, Kara A, Yuste I, *et al*. 3D printing technologies in personalized medicine, nanomedicines, and biopharmaceuticals. *Pharmaceutics*. 2023;15(2):313.
doi: 10.3390/pharmaceutics15020313

55. Wang P, Sun Y, Shi X, Shen H, Ning H, Liu H. 3D printing of tissue engineering scaffolds: a focus on vascular regeneration. *Bio-Des Manuf*. 2021;4(2):344-378.
doi: 10.1007/s42242-020-00109-0

56. Guerra AJ, Cano P, Rabionet M, Puig T, Ciurana J. 3D-printed PCL/PLA composite stents: towards a new solution to cardiovascular problems. *Materials (Basel)*. 2018;11(9):1679.
doi: 10.3390/ma11091679

57. Townsend JM, Hukill ME, Fung KM, *et al*. Biodegradable electrospun patch containing cell adhesion or antimicrobial compounds for trachea repair in vivo. *Biomed Mater*. 2020;15(2):025003.
doi: 10.1088/1748-605X/ab5e1b

58. Genden EM, Miles BA, Harkin TJ, *et al*. Single-stage long-segment tracheal transplantation. *Am J Transplant*. 2021;21(10):3421-3427.
doi: 10.1111/ajt.16752

59. Park JH, Ahn M, Park SH, *et al*. 3D bioprinting of a trachea-mimetic cellular construct of a clinically relevant size. *Biomaterials*. 2021;279:121246.
doi: 10.1016/j.biomaterials.2021.121246

60. Wahbeh JM, Lama J, Park S, Ebramzadeh E, Hollister SJ, Sangiorgio SN. Degradation and fatigue behavior of 3D-printed bioresorbable tracheal splints. *J Biomed Mater Res B Appl Biomater*. 2024;112(12):e35501.
doi: 10.1002/jbm.b.35501

61. Ji K, Zhang Q, Song W, *et al*. LncRNA PVT1 promotes cell proliferation, invasion, and migration and inhibits cell apoptosis by phosphorylating YAP. *Can J Gastroenterol Hepatol*. 2022;2022:5332129.
doi: 10.1155/2022/5332129

62. Li X, Ren H. Long noncoding RNA PVT1 promotes tumor cell proliferation, invasion, migration and inhibits apoptosis in oral squamous cell carcinoma by regulating miR-150-5p/GLUT-1. *Oncol Rep*. 2020;44(3):1101-1112.
doi: 10.3892/or.2020.7706

63. Cui M, Chang Y, Fang QG, *et al*. Non-coding RNA Pvt1 promotes cancer stem cell–like traits in nasopharyngeal cancer via inhibiting miR-1207. *Pathol Oncol Res*. 2019;25(4):1411-1422.
doi: 10.1007/s12253-018-0453-1

64. Du J, Zheng L, Gao P, *et al*. A small-molecule cocktail promotes mammalian cardiomyocyte proliferation and heart regeneration. *Cell Stem Cell*. 2022;29(4):545-558.e13.
doi: 10.1016/j.stem.2022.03.009